

This is a repository copy of New insights into combined thermal and vibration softening of magnesium alloy in rotational vibration assisted incremental sheet forming.

White Rose Research Online URL for this paper: https://eprints.whiterose.ac.uk/id/eprint/233215/

Version: Published Version

Article:

Zhu, H., Zeng, X. orcid.org/0000-0001-7074-9621, Long, H. orcid.org/0000-0003-1673-1193 et al. (1 more author) (2025) New insights into combined thermal and vibration softening of magnesium alloy in rotational vibration assisted incremental sheet forming. Journal of Magnesium and Alloys. ISSN: 2213-9567

https://doi.org/10.1016/j.jma.2025.09.016

Reuse

This article is distributed under the terms of the Creative Commons Attribution (CC BY) licence. This licence allows you to distribute, remix, tweak, and build upon the work, even commercially, as long as you credit the authors for the original work. More information and the full terms of the licence here: https://creativecommons.org/licenses/

Takedown

If you consider content in White Rose Research Online to be in breach of UK law, please notify us by emailing eprints@whiterose.ac.uk including the URL of the record and the reason for the withdrawal request.



JID: JMAA ARTICLE IN PRESS [m5+;October 16, 2025;1:54]

KeAi

CHINESE ROOTS
GLOBAL IMPACT

Available online at www.keaipublishing.com/en/journals/journal-of-magnesium-and-alloys/

ScienceDirect

Journal of Magnesium and Alloys xxx (xxxx) xxx



www.elsevier.com/locate/jma

Full Length Article

New insights into combined thermal and vibration softening of magnesium alloy in rotational vibration assisted incremental sheet forming

Hui Zhu^a, Xiaohan Zeng^b, Hui Long^{a,*}, João Quinta da Fonseca^b

^a School of Mechanical, Aerospace and Civil Engineering, The University of Sheffield, Sheffield S13JD, UK

^b Department of Materials, The University of Manchester, Manchester M139PL, UK

Received 9 June 2025; received in revised form 7 September 2025; accepted 23 September 2025 Available online xxx

Abstract

With the generation of both localised thermal and vibration in incremental sheet forming (ISF) by novel tool designs, rotational vibration assisted ISF (RV-ISF) can achieve significant force reduction and material softening. However, the combined thermal and vibration softening in RV-ISF is unclear. By evaluating the similarities and differences of friction stir ISF (FS-ISF) and RV-ISF, this study develops a novel approach to decouple and quantify the thermal and vibration softening effects in RV-ISF of AZ31B-H24, providing new insights into underlying thermal and vibration softening mechanism. Experimental results reveal that in RV-ISF of AZ31B-H24 the thermal softening due to frictional heating dominates with $45 \sim 65\%$ of softening, while the vibration effect only contributes up to 15% of softening, from the conventional ISF, depending on the tool designs and tool rotational speed. The double-offset tool (T2) produces greater vibration softening than the three-groove tool (T3) owing to the higher vibration amplitude of the T2 tool. An increase in tool rotational speed primarily enhances thermal softening with only marginal changes to the vibration effect. Microstructural analysis suggests that with average grain size of 0.94 µm at the top layer, RV-ISF with T3 and 3000 rpm is more effective for microstructure refinement than that by FS-ISF, especially on the tool-sheet contact surface, which confirms the occurrence of surface shearing. This refinement is a result of the reduced recrystallisation degree, 71.8% at the top bottom layer. Compared with FS-ISF, RV-ISF can lead to not only higher geometrically necessary dislocation density, but also higher fraction of low-angle grain boundaries, indicating that softening mechanism due to localised vibration effect is resulted from the enhanced rearrangement and annihilation of dislocations. These findings contribute to new understanding of the thermal and vibration softening effects in RV-ISF of AZ31B-H24 and offer a theoretical foundation for the tool design and process optimisation. © 2025 Chongqing University. Publishing services provided by Elsevier B.V. on behalf of KeAi Communications Co. Ltd. This is an open access article under the CC BY license (http://creativecommons.org/licenses/by/4.0/)

Keywords: Incremental sheet forming; Magnesium alloy; Vibration softening; Thermal softening; Microstructure evolution.

1. Introduction

Magnesium alloys, particularly AZ31B, are widely applicable in lightweight engineering due to their high specific strength, damping capacity, and recyclability, making them significant in aerospace, automotive, and biomedical appli-

E-mail addresses: huizhucn@outlook.com (H. Zhu), xiaohan.zeng@manchester.ac.uk (X. Zeng), h.long@sheffield.ac.uk (H. Long), joao.fonseca@manchester.ac.uk (J. Quinta da Fonseca).

cations [1–3]. In recent years, numerous studies have been reported aiming to enhance the performance of magnesium alloys. Momeni et al. [4] revealed that precipitation hardening of ZK60Gd reinforced with 5–10 wt% SiC improves hardness and wear resistance by altering key wear mechanisms, with 10 wt% SiC showing the best performance. While for AZ31, the addition of 5–20 wt% bimodal size B₄C can improve the wear resistance, with 10 wt% B₄C showing optimal performance [5]. However, the strong texture and plastic anisotropy cause limited ductility and formability of the material [6,7]. This intrinsic challenge has prompted extensive research into advancing forming techniques capable of overcoming these

https://doi.org/10.1016/j.jma.2025.09.016

2213-9567/© 2025 Chongqing University. Publishing services provided by Elsevier B.V. on behalf of KeAi Communications Co. Ltd. This is an open access article under the CC BY license (http://creativecommons.org/licenses/by/4.0/)

[☆] Peer review under the responsibility of Chongqing University

^{*} Corresponding author.

Nomencla	furo	10	Motorial strain hardoning exponent in the ser
Nomencia	ture	n	Material strain hardening exponent in the constitutive model
Symbol	Term (Unit)	C	Strain rate sensitivity exponent in the consti-
r	Distance from the studied position to the tool centre (mm)	T^*	tutive model Homologous temperature in the constitutive
arphi	Angle from the studied position to the tool	T	model Temperature in the constitutive model (K)
θ	rotational axis (rad) Angle from workpiece meridional cross-	T_0	Reference temperature in the constitutive
	section to studied position (rad)	$T_{ m melt}$	model (K) Melting temperature (K)
r_{tool}	Radius of the forming tool (mm) Sheet thickness of the contact area (mm)	C_0, C_1, C_2	Material constants to reflect the temperature
t_0	Initial sheet thickness (mm)		dependence of strain rate in the constitutive
$t_{ m m}$	Mean thickness (mm)	$K_{\mathrm{T-FS}}$	model Thermal softening coefficient in FS-ISF
$t' \ \Delta t$	Sheet thickness after the last contact (mm) Thickness reduction from the last contact to	$K_{\mathrm{T-RV}}$	Thermal softening coefficient in RV-ISF
	the current contact (mm)	$K_{ m Vib}$ F	Vibration softening coefficient in RV-ISF Vertical forming force (N)
lpha eta	Actual drawing angle (rad) Indentation angle in the workpiece meridional	F_{FS}	Vertical forming force in FS-ISF (N)
P	direction (rad)	$F_{ m RV}$	Vertical forming force in RV-ISF (N)
β_1	Angle induced by forming tool increment in	$F_{ m C} \ \Delta F$	Vertical forming force in C-ISF (N) Vertical forming force reduction (N)
$arepsilon_{ m m}$	workpiece meridional direction (rad) Mean equivalent plastic strain of the contact	$\Delta F_{\mathrm{T-FS}}$	Vertical forming force reduction due to ther-
	area	$\Delta F_{ m T-RV}$	mal effect in FS-ISF (N) Vertical forming force reduction due to ther-
${arepsilon_{ m m}}'$	Mean equivalent plastic strain after the last contact		mal effect in RV-ISF (N)
$\varepsilon_{ m max}$	Maximum equivalent plastic strain of the contact area	$\Delta F_{ m Vib}$	Vertical forming force reduction due to vibration effect in RV-ISF (N)
${arepsilon_{max}}'$	Maximum equivalent plastic strain after the	$\Delta\sigma_{\mathrm{m}}$	Mean equivalent stress reduction (MPa) Tensile stress reduction due to thermal effect
τ	last contact Duration time for the completion of deforma-	$\Delta\sigma_{ m T}$	(MPa)
	tion in the current contact (s)	$\Delta\sigma_{ m Vib}$	Tensile stress reduction due to vibration effect (MPa)
$arphi \ \dot{arepsilon}_{ m m}$	Feed rate (mm/min) Mean strain rate of the localised deformation	F_{FS3000}	Vertical forming force in FS-ISF with 3000 rpm (N)
$\dot{arepsilon}_{ m max}$	in ISF (s ⁻¹) Maximum strain rate of the localised defor-	$\sigma_{\mathrm{T-FS}}$	Material flow stress at the temperature
σ.	mation in ISF (s ⁻¹) Mean equivalent stress in the constitutive	$\sigma_{\mathrm{T-FS3000}}$	recorded in FS-ISF (MPa) Material flow stress at the temperature
$\sigma_{ m m}$	model (MPa)		recorded in FS-ISF with 3000 rpm (MPa)
σ_0	Flow stress at reference strain rate and tem-	$\sigma_{ m T-RV}$	Material flow stress at the temperature recorded in RV-ISF (MPa)
ε	perature Equivalent plastic strain in the constitutive model	$\sigma_{ m room}$	Material flow stress at room temperature in C-ISF (MPa)
$\dot{\varepsilon}^*$	Homologous strain rate in the constitutive model	$\Delta F_{\mathrm{T-FS-RV}}$	Difference of vertical forming force due to the temperature difference in FS-ISF and RV-ISF
arepsilon	Strain rate in the constitutive model (s^{-1})	0	with the same rotational speed (N) Dislocation density (mm ⁻²)
$\dot{arepsilon}_0$	Reference strain rate in the constitutive model (s^{-1})	$ ho \gamma$	Constant correlating with the geometry of the
\boldsymbol{A}	Initial yield strength at reference strain rate in	9	grain boundaries Mean KAM (Radians)
В	the constitutive model (MPa) Material constant in the constitutive model	и	EBSD step size (μm)
	(MPa)	b	Magnitude of the Burgers vector (nm)

limitations while maintaining material integrity and improving formability. To address this, Tayebi et al. [8] revealed that the microalloying Mg-Al-Mn alloy with Zr and Sc, processed by extrusion, can refine the microstructure, enhance the mechanical strength and ductility obviously. Zhang et al. [9] revealed that the electrical pulse-ultrasonic treatment of AZ31 Mg sheets can promote the dynamic recrystallisation and reduce the deformation resistance, enhancing formability. In the forming of magnesium alloy sheets, including AZ31B sheets, conventional sheet forming methods, such as stamping, deep drawing, and hydroforming, often require elevated temperatures to enhance the ductility of AZ31B sheets by activating non-basal slip systems and grain boundary shearing [10]. While these approaches partially address formability issues, significant drawbacks are introduced, including high energy consumption and grain coarsening [11]. Additionally, the need for expensive dedicated dies and tooling makes these methods economically impractical for small-batch or customised production. These limitations highlight the necessity for developing innovative forming strategies that combine process flexibility, cost-effectiveness, and material performance. Incremental sheet forming (ISF) has emerged as a flexible dieless forming process that overcomes many limitations of traditional sheet forming methods. By deforming sheets incrementally using a computer numerical controlled tool, ISF improves the formability of sheet materials and eliminates the need for dedicated dies, enabling rapid prototyping and costeffective customisation [12,13]. To further enhance the feasibility of ISF in processing hard-to-form materials including AZ31B, heat-assisted ISF is usually used. Zhang et al. [14] developed a new warm ISF processing method with oil bath heating to improve the formability of AZ31B. Duflou et al. [15] and Lehtinen et al. [16] developed laser-assisted ISF using a laser beam to locally heat the sheet metal to enhance the formability and forming accuracy. Al-Obaidi et al. [17], Ambrogio et al. [18] and Li et al. [19] developed induction heat-assisted ISF by employing electromagnetic induction for efficient contactless heating. Fan et al. [20] developed electric hot ISF and electropulsing assisted ISF to heat the sheet by creating electric current, which is ideal for high-strength alloys, while Ao et al. [21] reported that in the developed electropulsing assisted ISF, the electropulsing had an effect on the weakening of anisotropy behaviours of Ti-6Al-4 V as well as the appearance of dynamic recovery, dynamic recrystallisation and phase transformation structure. Zhang et al. [22] applied the electric hot ISF in forming AZ31B sheet and revealed that Joule heating promotes dynamic recrystallisation, enhancing formability through the transition from twinning/slip to dynamic recrystallisation. Otsu et al. [23] developed friction stir ISF (FS-ISF) by utilizing friction heating from a rotating tool to soften the material locally. Zhan et al. [24] proposed a new two-stage FS-ISF to achieve microstructure uniformity and enhancement of mechanical properties in aluminium alloys. Zhu and Ou [25] developed heat-assisted FS-ISF with flexible heating tapes to heat the bottom surface of the sheet while the tool-sheet friction to heat the top surface of the sheet to achieve a uniform through-thickness temperature distribution.

However, heat-assisted ISF is usually not energy-efficient, considering the low heat exchange efficiency.

Apart from the heating effect, the vibration effect also has benefit to the material softening and the formability improvement in ISF process. Vahdati et al. [26], for the first time, proposed ultrasonic vibration assisted ISF (UV-ISF), which helps in reducing the average vertical forming force and springback. The UV-ISF is beneficial for forming high-strength sheet metals and lightweight alloys. Besides the forming force reduction, Amini et al. [27] reported that the use of ultrasonic vibration in the ISF process can also improve the material formability. Li et al. [28] confirmed that the ultrasonic vibration can reduce the forming force and improve the surface quality of ISF. Li et al. [29] found that after applying ultrasonic vibration, the material flow area increased dramatically, with the vibration amplitude having a much greater effect than the vibration frequency, which is similar with the acoustic softening effect. Long et al. [30] found that the materials with higher yield stress tend to experience more substantial forming force reduction and a greater temperature rise, and that increasing ultrasonic power or reducing the tool feed speed further amplifies these effects. The authors also found that with higher vibration amplitude, the smaller tools can also achieve force reduction and temperature rise effect similar to that by larger tools. Cheng et al. [31] built up a finite element (FE) simulation method to simulate the high-frequency vibration in UV-ISF with development of a hybrid constitutive model combining the phenomenological, thermal activation and dislocation annihilation models. In their study, it was revealed that with the presence of relatively larger grains coupled with an increase in low-angle grain boundaries (LAGBs), it was suggested that ultrasonic vibrations trigger dynamic recovery in the material. However, UV-ISF requires an additional ultrasonic generator, increasing the complexity and cost of the

By providing tool rotation, the same as that in FS-ISF, but with novel tool designs, Lu et al. [32], Wu et al. [33], Dewangan et al. [34] and Long et al. [35] proposed a new ISF variant with tool rotation induced vibration (V-ISF) or rotational vibration assisted ISF (RV-ISF) to generate both thermal and vibration effect in localised deformation area. The tools developed by Lu et al. [32] have single or double offset but with round or curved surface shapes. The tool rotation induced vibration leads to the large surface shear deformation, the microstructure refinement and the enhanced material hardness of AZ31B. The tool developed by Wu et al. [33] has a flat bottom surface but different radius on different surface sides. This tool also increased the surface shear deformation, and promoted the formability improvement of AA5052, although the friction heat and temperature rise were reduced. Dewangan et al. [34] designed an en-grooved hemispherical tool with circular shank, a hemispherical tool with elliptical shank, and a hemispherical tool with triangular shank to generate vibration effect in the ISF tests. Differently, Long et al. [35] developed new rosette tools with grooves on the hemispherical tool surface for better deformation stability. The localised temperature rise leads to the improvement of material formability and the reduction of the material flow stress of AZ31B, while the localised vibration leads to further material softening [35].

To understand the vibration softening effect and mechanism, Langenecker [36] found that the ultrasonic vibration can achieve similar effect as that by temperature elevation for force reduction in plastic deformation, and proposed that the concentrated energy from ultrasonic vibration is absorbed by the material internal microstructures such as dislocations, voids, and grain boundaries, which in turn facilitates the initiation of dislocation slip. Daud et al. [37] proposed that the softening effect induced by ultrasonic vibration is the result of a coupled mechanism involving both acoustic softening and stress superposition. Siu et al. [38] reported that the ultrasonic vibration distinctly enhances the subgrain formation in the ultrasonic vibration assisted micro-indentation test of aluminium, which far exceeds the effect attributable solely to the generated heat by the ultrasonic vibration. This phenomenon is attributed to the capacity of ultrasonic vibration to promote dipole annihilation, as it induces dislocations to move intermittently over longer distances, increasing the likelihood of encountering and annihilating dipole pairs. By performing an ultrasonic vibration assisted tensile test of low-carbon steel, Dutta et al. [39] found reductions in both dislocation density and the fraction of LAGBs. This effect is attributed to the preferential absorption of ultrasonic energy by local areas such as dislocations, vacancies, and grain boundaries, which requires less energy to achieve the same softening effect compared to thermal assistance. Apart from employing high frequency ultrasonic vibration in forming, superimposing low-frequency vibration onto the forming process can also reduce the forming load [40]. Lin et al. [41] revealed that the low-frequency vibration enhances dislocation movement and grain rotation in the upsetting of titanium alloy, leading to dislocation annihilation within shear bands while promoting dislocation accumulation and formation of LAGBs near grain boundaries in regions of high-degree deformation. Sun et al. [42] also reported that superimposing low-frequency vibration provides extra kinetic energy that drives microstructural evolution during deformation of aluminium alloy and enhances dislocation distribution: at vibration amplitudes below the length of elastic deformation zone, cyclic elastic energy fosters dislocation diffusion and proliferation, whereas above the length of elastic deformation zone, the dislocation annihilation can be accelerated by the cyclic plastic deformation energy. However, current studies about the vibration softening are mainly focused on simple deformation conditions without considering the complexity of deformation in the practical forming process as well as new sheet forming processes such as RV-ISF.

Despite these studies about vibration softening effect and mechanism, it is still not understood that the material softening behaviour in RV-ISF process of AZ31B with coupled cyclic and localised deformation under friction heating and vibration effects. This creates a complex deformation condition for evaluating individual and combined softening effects and mechanisms in RV-ISF. This study bridges these gaps

and systematically investigates the combined effects of friction heat and vibration in the softening and microstructure evolution of AZ31B in RV-ISF by applying different tool designs in FS-ISF and RV-ISF processing. New contributions of this study are: (1) decoupling of thermal and vibration softening effects to better understand their individual contributions and underlying mechanisms by developing an analytical model to calculate the softening coefficients in RV-ISF; (2) revealing microstructure evolution under the complex deformation condition in RV-ISF and FS-ISF, and the identification of the mechanism of vibration softening effect. This study advances the understanding of the thermal and vibration softening effect and mechanism in RV-ISF and provides a solid foundation for new tool design and process optimisation in ISF and RV-ISF.

2. Material and methods

2.1. Material

AZ31B-H24 sheets with thickness of 1 mm used in this study met the requirement set by the American Society for Testing and Material (standard: ASTM-B90). The chemical compositions of AZ31B were given by the supplier shown in Tables 1, while the H24 stands for the partially annealed and partially strain hardened treatment state. The sheets were cut into 150 mm \times 150 mm squared pieces for the tests.

2.2. RV-ISF principle and experimental setup

Fig. 1 provides illustrations of the FS-ISF and RV-ISF processes and the formed geometry used in this study. In FS-ISF as shown in Fig. 1(c), the localised deformation is produced by a rotating hemispherical tool with localised temperature rise from the significant friction heating effect, while in the developed RV-ISF as shown in Fig. 1(d) and (e), a double-offset tool (T2) or a three-groove tool (T3) is rotated to generate mechanical vibration effect in addition to the localised temperature rise from the friction heating effect and the negligible vibration heating effect [43-45]. As illustrated in Fig. 1(f) and (g), the T2 is an elliptical tool with reduced distance from the tool rotational centre to the sheet surface on two opposite sides of the tool, while the T3 has three grooves uniformly around the circumferential direction of the tool, which results in no direct contact between the tool and sheet, and allows reduced distance from the tool centre to the sheet surface. The local sheet alternately experiences elastic deformation and springback, in addition to plastic deformation, when the tool rotates, inducing mechanical vibration effect. Compared with the T2 and the four-groove tool (T4) used in the previous study [35], the newly developed T2 used in this study had a reduced offset of 0.2 mm instead of 1 mm to reduce the vibration amplitude and increase the deformation stability, and the newly developed T3 reduced the number of grooves to increase the contact area

Table 1 Chemical compositions of AZ31B-H24 sheets.

Al	Cu	Mn	Zn	Ca	Ni	Be	Si	Fe	Other	Mg
3.17	0.0010	0.40	1.03	0.0010	0.0010	< 0.0010	0.014	0.0027	< 0.30	Bal.

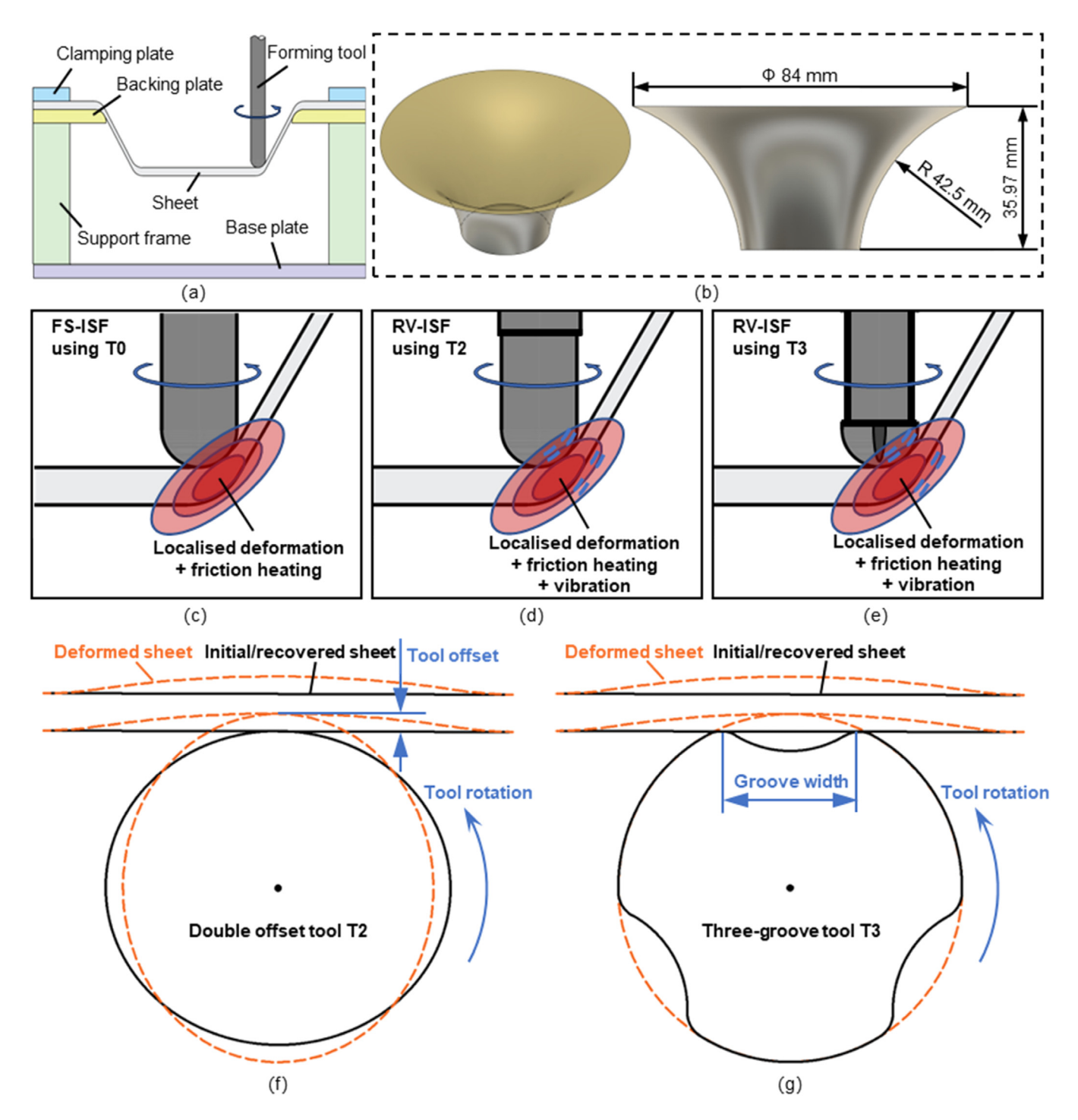
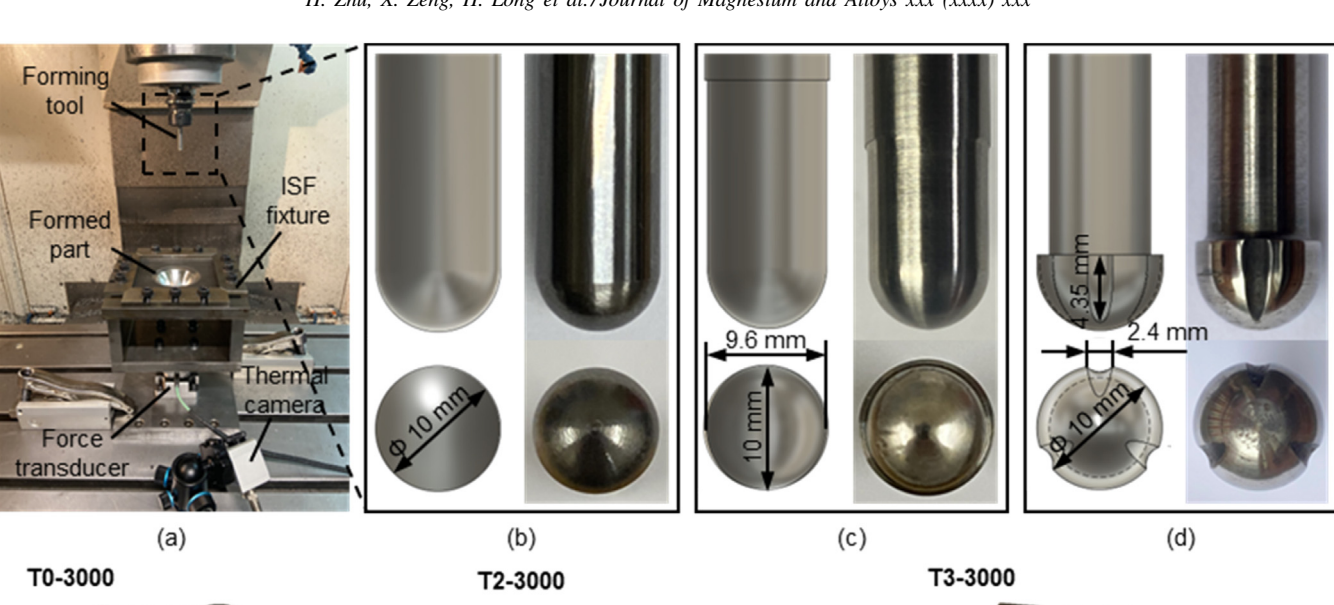


Fig. 1. Illustration of ISF variants used in this study. (a) ISF setup. (b) Test geometry of hyperbolic truncated cone. (c) FS-ISF. (d) RV-ISF using T2. (e) RV-ISF using T3. (f) Illustration of vibration induction of double offset tool T2. (g) Illustration of vibration induction of three-groove tool T3.



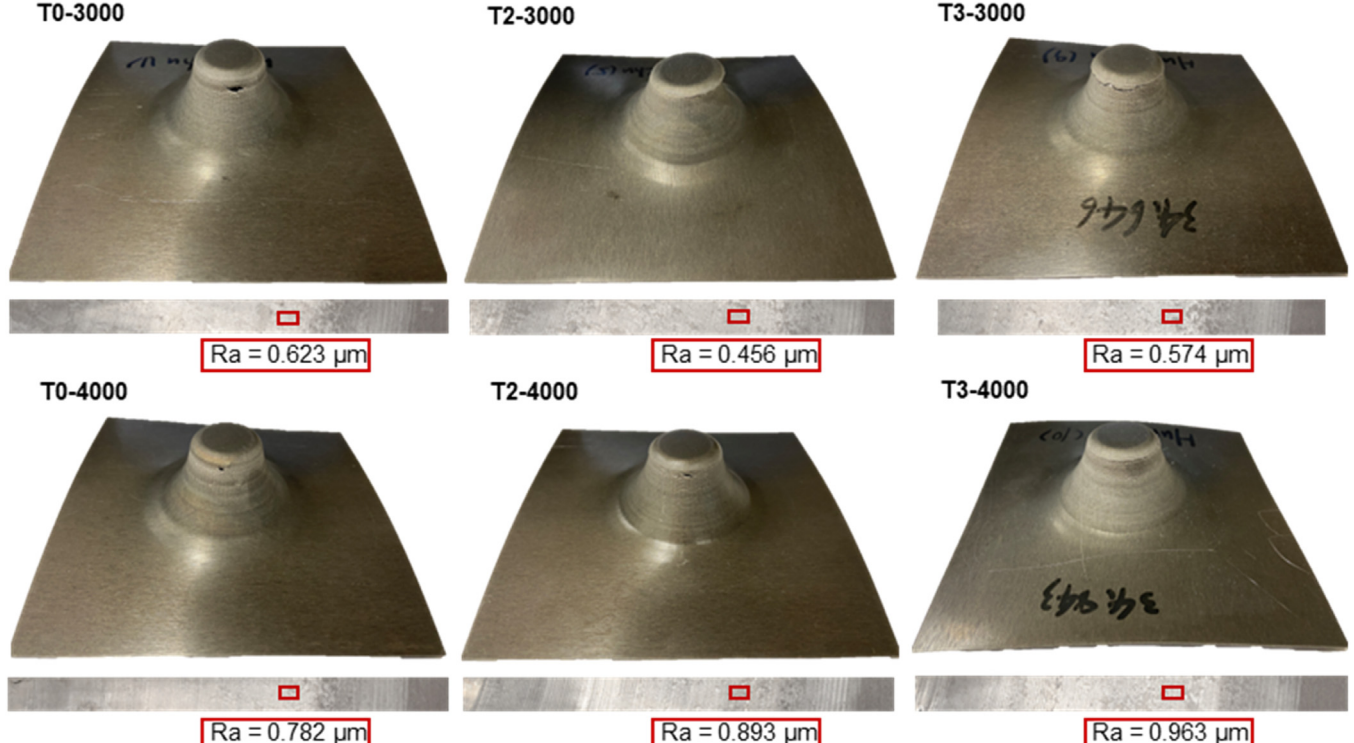


Fig. 2. Experimental setup, forming tools and formed parts of FS-ISF and RV-ISF. (a) Experimental setup including forming and measurement systems. (b) Conventional hemispherical tool T0. (c) Double-offset tool T2 with 0.2 mm offset on both sides. (d) Three-groove tool T3 with grooves on the tool surface. (e) Images of formed conic parts by FS-ISF and RV-ISF and locally scanned tool-sheet contact surface and surface roughness from the bottom of formed parts at a drawing angle of 40°.

to enhance friction heat generation. Fig. 2(b)–(d) shows the designs and dimensions of different tools employed in this study.

6

As shown in Fig. 2(a), during the test, the forming temperature on the sheet bottom surface of the formed hyperbolic cone geometry was captured by an infrared thermal camera (model: MICRO-EPSILON TIM160), while the 3-axis forming forces were recorded by a force transducer (model: Kistler 9367C). Each test was stopped manually if the fracture hap-

pened or ran until the end if without fracture. The formed hyperbolic cone parts are shown in Fig. 2(e). The localised toolsheet contact surface was scanned and the surface roughness at drawing angle of 40° was measured by a surface roughness tester (model: Bruker Alicona InfiniteFocus) with vertical resolution of 0.5 μm and lateral resolution of 5 μm . T2 and T3 tools produced better surface finish than the conventional T0 tool with 3000 rpm, while yielded worse surface finish with 4000 rpm.

Table 2 Process parameters for FS-ISF and RV-ISF of AZ31B-H24.

Test ID	Tool	Rotational speed (rpm)	Reference vibration frequency (Hz)	Measured vibration frequency (Hz)	Measured vibration amplitude at a drawing angle of 40° (μm)	
T0-3000	T0	3000	N/A	N/A	N/A	
T0-4000	T0	4000	N/A	N/A	N/A	
T2-3000	T2	3000	100	97.66	24.32	
T2-4000	T2	4000	133.33	132.81	29.18	
T3-3000	T3	3000	150	148.44	6.26	
T3-4000	T3	4000	200	199.22	8.19	

2.3. RV-ISF experimental design

As shown in Fig. 1(b), a hyperbolic truncated cone shape with increasing wall angle from 22° to 85° was designed to achieve the change of tool-sheet contact area and thickness reduction. To explore the thermal and vibration effect on the forming force reduction, T0, T2 and T3 with rotational speeds of 3000 and 4000 rpm were used, as listed in Table 2. Measured by an Eddy current sensor (model: MICRO-EPSILON CSH1-CAm1) and processed by the fast Fourier transform (FFT), the vibration frequencies and amplitudes at the drawing angle of 40° were obtained and are given in Table 2. For all the tests, the step size of the toolpath was 0.3 mm, while the feed rate was 1000 mm/min. No lubricant was used to maximize friction between forming tool and sheet surface for the promoted heat generation to improve the material formability of AZ31B-H24.

2.4. Tensile testing at elevated temperatures

The uniaxial tensile tests were conducted on the thermal mechanical testing system (model: Gleeble 3800) with the suggested specimen design detailed in Section 3.2. The testing temperatures of 22, 50, 100, 150, 200, 250, 300, 350, 400 and 450 °C were used for obtaining the tensile flow stress curves, while strain rates of 0.1, 1 and 10 s⁻¹ were used based on the analysis of strain rate in ISF presented in Section 3.1. The specimens were heated by resistance heating and the temperature was measured by thermal couple at the middle position. The stress and strain were measured at the ends of specimens by the testing machine.

2.5. Microstructural analysis using electron back-scatter diffraction (EBSD)

Two samples were selected and prepared for EBSD analysis: T0–3000 and T3–3000. The specimens were cold-mounted and ground with SiC paper from 320 to 4000 grit, followed by diamond polishing with 3 μ m and 1 μ m diamond suspension and 0.2 μ m fumed silica. After manual preparation, the sample was then taken out from the cold mounting resin and mounted on an aluminium stub for scanning electron microscope (SEM) with silver paint. Before the EBSD scan, ion beam milling was carried out on the samples to

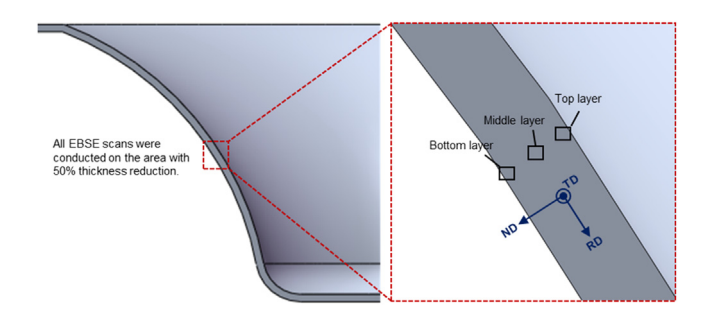


Fig. 3. Illustration of the EBSD scanning areas.

clean the sample surface and further polish it to achieve a flat and scratch-free surface on an ion beam milling system (model: Leica EM RES102). The sample was cleaned with 7 kV, 2.8 mA, 12.5° gun angle and milling angle for 1.5 h, followed by the polishing step with 5° gun angle and milling angle for 2 h.

The analysis of the EBSD scans was carried out in a field emission gun-SEM (FEG-SEM, model: ThermoFisher Apreo) equipped with Oxford Instrument Symmetry 3 detector. The EBSD parameters were 20 kV voltage, 26 nA current, and 20 mm working distance. The step size was 1 μ m for the non-deformed area and 0.1–0.15 μ m for the deformed area through the sheet thickness. Measurements were conducted at the thickness reduction of 50% of the formed cone geometry. As shown in Fig. 3, three areas were analysed: the top region near the tool-sheet contact surface, the middle region, and the bottom region of the sheet thickness. In the analysis, the rolling direction (RD), transverse direction (TD) and normal direction (ND) were defined as along the meridional, circumferential and through-thickness directions of the ISF formed hyperbolic cone part, respectively.

3. Modelling of thermal and vibration softening in RV-ISF

To decouple the contributions of thermal and vibration softening effects, analytical method is used considering the difficult-to-determine stress-strain curves under vibration effect at high temperature, and the difficulty in FE simulation of the friction heating and chipping effect at the tool-sheet contact interface, which requires a prohibitively fine mesh and huge computing resources and time.

H. Zhu, X. Zeng, H. Long et al./Journal of Magnesium and Alloys xxx (xxxx) xxx

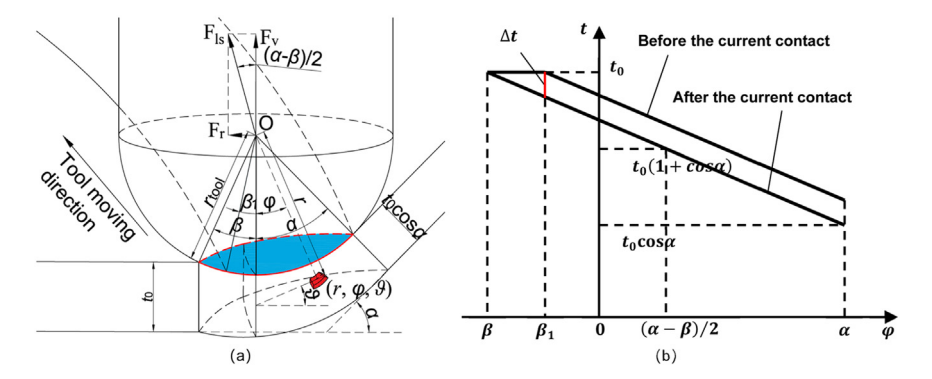


Fig. 4. Illustration of localised deformation in ISF. (a) Local coordinate system of the contact area in three-dimensional view. (b) Linear thickness distribution and thickness reduction.

3.1. Analysis of localised material deformation and strain rate in ISF

The material deformation in ISF is analysed in a localised spherical coordinate system. As shown in Fig. 4(a), the origin of the coordinates is located at the tool centre, O, and any position within the contact area can be located as (r, φ, θ) . r is the distance from the sheet surface to the tool centre, and r equals the tool radius r_{tool} on the tool-sheet contact interface; φ is the angle to the tool rotational axis; θ is the angle to the workpiece meridional cross-section. In Fig. 4(a), t_0 is the initial sheet thickness; α is the drawing angle; β is the indentation angle in the workpiece meridional direction; β_1 is the angle induced by the increment of forming tool in the workpiece meridional direction.

According to the assumption of linear distribution, as illustrated in Fig. 4(b), the thickness distribution of the workpiece meridional cross-section from the initial thickness t_0 to the forming wall thickness $t_0\cos\alpha$ is given as following:

$$t = t_0 - \frac{t_0(1 - \cos\alpha)(\beta + \varphi\cos\theta)}{\alpha + \beta} \tag{1}$$

where $\theta = 0$ or $\theta = \pi$.

8

For simplification, the thickness at the middle position of the meridional cross-section is assumed as the mean thickness $t_{\rm m}$ of the contact area to represent the overall thickness value. The value of $t_{\rm m}$ is calculated as following:

$$t_{\rm m} = \frac{1}{2}t_0(1+\cos\alpha) \tag{2}$$

With the thickness reduction compared with the initial sheet, the mean equivalent plastic strain ε_m corresponding to the mean thickness and the maximum equivalent plastic strain ε_{max} of the contact area are calculated as following considering the local deformation state as biaxial tension condition:

$$\varepsilon_{\rm m} = 2 \ln \frac{2}{1 + \cos \alpha} \tag{3}$$

$$\varepsilon_{\text{max}} = 2 \ln \frac{1}{\cos \alpha} \tag{4}$$

Before getting into the current contact and subjecting to further deformation, the thickness t' after the last contact is calculated from the last tool-sheet contact as following:

$$t' = t + \Delta t \tag{5}$$

where Δt is the thickness reduction from the last contact to the current contact. According to the assumption of linear thickness distribution as illustrated in Fig. 4(b), Δt is consistent in the whole contact area thus can be calculated as the thickness reduction from t_0 where $\varphi = \beta_1$:

$$\Delta t = t_0 \frac{(1 - \cos \alpha)(\beta - \beta_1)}{\alpha + \beta} \tag{6}$$

The mean and the maximum equivalent plastic strains ($\varepsilon_{\rm m}{}'$ and $\varepsilon_{\rm max}{}'$) after the last tool contact are then given as following:

$$\varepsilon_{m}' = 2 \ln \frac{2(\alpha + \beta)}{(1 + \cos \alpha)(\alpha + \beta) + 2(1 - \cos \alpha)(\beta - \beta_1)}$$
 (7)

$$\varepsilon_{\text{max}}' = 2 \ln \frac{\alpha + \beta}{\cos \alpha (\alpha + \beta) + (1 - \cos \alpha)(\beta - \beta_1)}$$
 (8)

To create the thickness reduction and equivalent strain increment, the duration time τ for the completion of deformation in the current contact can be approximated as the division of the length of the contact area in the circumferential direction of the workpiece by the tool moving feed rate υ :

$$\tau = \frac{r_{\text{tool}}\sqrt{(\sin\beta)^2 - (\sin\beta_1)^2}}{(9)}$$

Then, the mean and the maximum strain rates ($\dot{\varepsilon}_m$ and $\dot{\varepsilon}_{max}$) of the localised deformation can be calculated as the division of the equivalent strain increment by the duration time τ of the contact:

$$\dot{\varepsilon}_{\rm m} = \frac{\varepsilon - \varepsilon'}{\tau} = \frac{2\upsilon \ln\left[1 + \frac{2(1 - \cos\alpha)(\beta - \beta_1)}{(1 + \cos\alpha)(\alpha + \beta)}\right]}{r_{\rm tool}\sqrt{(\sin\beta)^2 - (\sin\beta_1)^2}}$$
(10)

(4)
$$\dot{\varepsilon}_{\text{max}} = \frac{\varepsilon - \varepsilon'}{\tau} = \frac{2\upsilon \ln\left[1 + \frac{(1 - \cos\alpha)(\beta - \beta_1)}{\cos\alpha(\alpha + \beta)}\right]}{r_{\text{tool}}\sqrt{(\sin\beta)^2 - (\sin\beta_1)^2}}$$
(11)

Please cite this article as: H. Zhu, X. Zeng, H. Long et al., New insights into combined thermal and vibration softening of magnesium alloy in rotational vibration assisted incremental sheet forming, Journal of Magnesium and Alloys, https://doi.org/10.1016/j.jma.2025.09.016

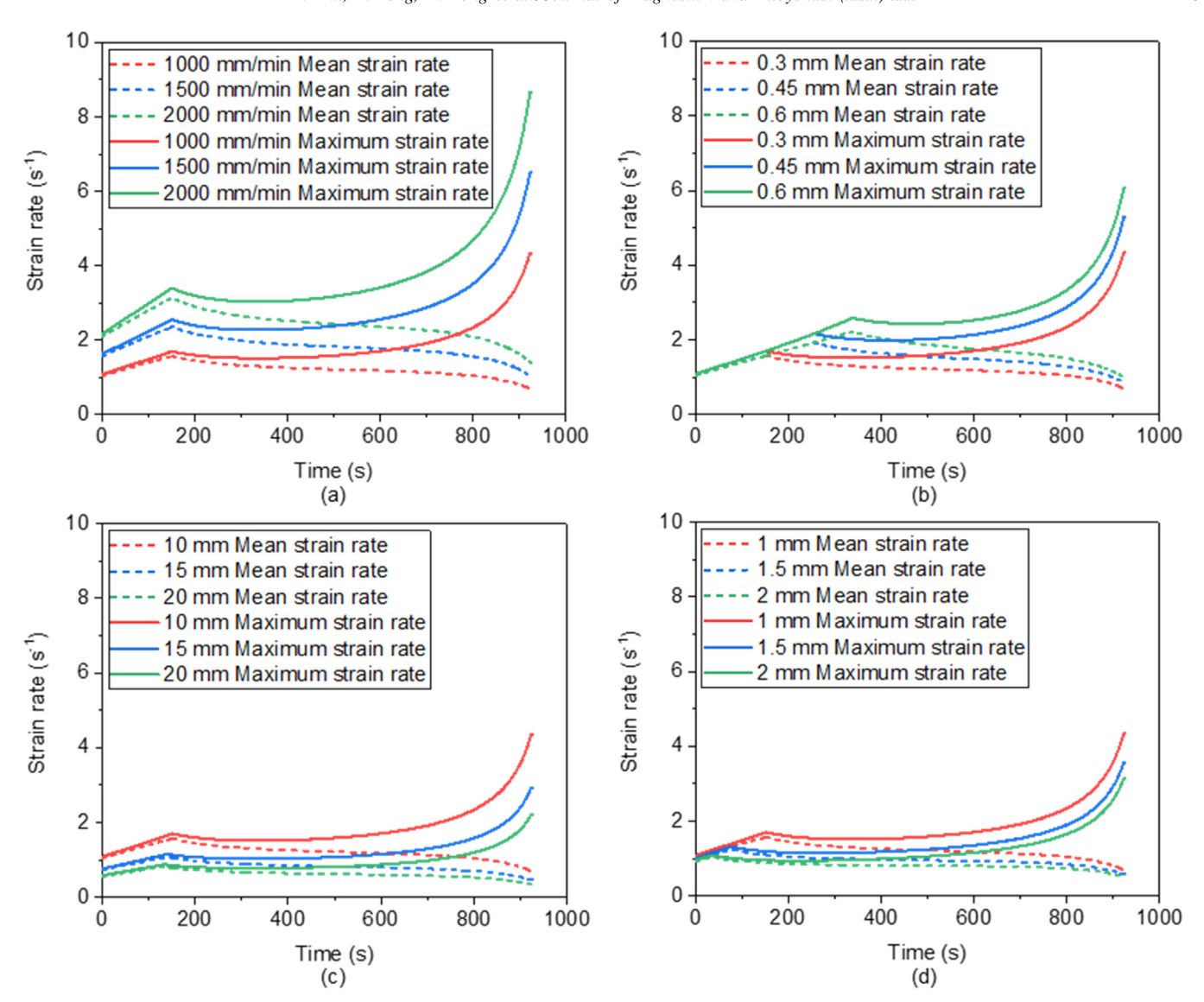


Fig. 5. Modelling of strain rate evolution in FS-ISF and RV-ISF of the hyperbolic truncated cone part. (a) With different feed rates. (b) With different step sizes. (c) With different tool diameters. (d) With different sheet thicknesses.

Based on Eqs. (10) and (11), the mean and the maximum strain rates in ISF processes with different feed rates, step sizes, tool dimensions and sheet thicknesses are calculated as shown in Fig. 5. For comparison, the base case of ISF process has a feed rate of 1000 mm/min, a step size of 0.3 mm, a tool diameter of 10 mm and a sheet thickness of 1 mm. It is observed that the feed rate has the most significant effect on the strain rate, followed by the step size, while the tool size and sheet thickness only have minor effects. It is noteworthy that with the same feed rate, step size, tool size and sheet thickness, different tool designs are considered to have the same strain rate in localised plastic deformation as the tool rotation only applies small amplitudes on the sheet material, which limit the local vibration effect within elastic deformation stage. This provides the strain rate range for the material tensile testing and the constitutive modelling of the flow stress, which are essential to the evaluation of force reduction and softening behaviour in forming AZ31B-H24.

3.2. Constitutive modelling of AZ31B-H24 over the identified range of strain rates and temperatures

To evaluate the material deformation and the thermal softening effect at elevated temperatures, constitutive modelling for flow stress prediction of AZ31B-H24 at different temperatures and strain rates is developed. As presented by the dotted curves in Fig. 6, the flow stress curves at strain rates of $0.1-10~\rm s^{-1}$ and temperatures of 22–450 °C are used for the modelling.

The effect of plastic strain on the flow stress follows the formulation of Johnson-Cook (JC) model [46], and the effect of strain rates follows the formulation of Fields-Backofen

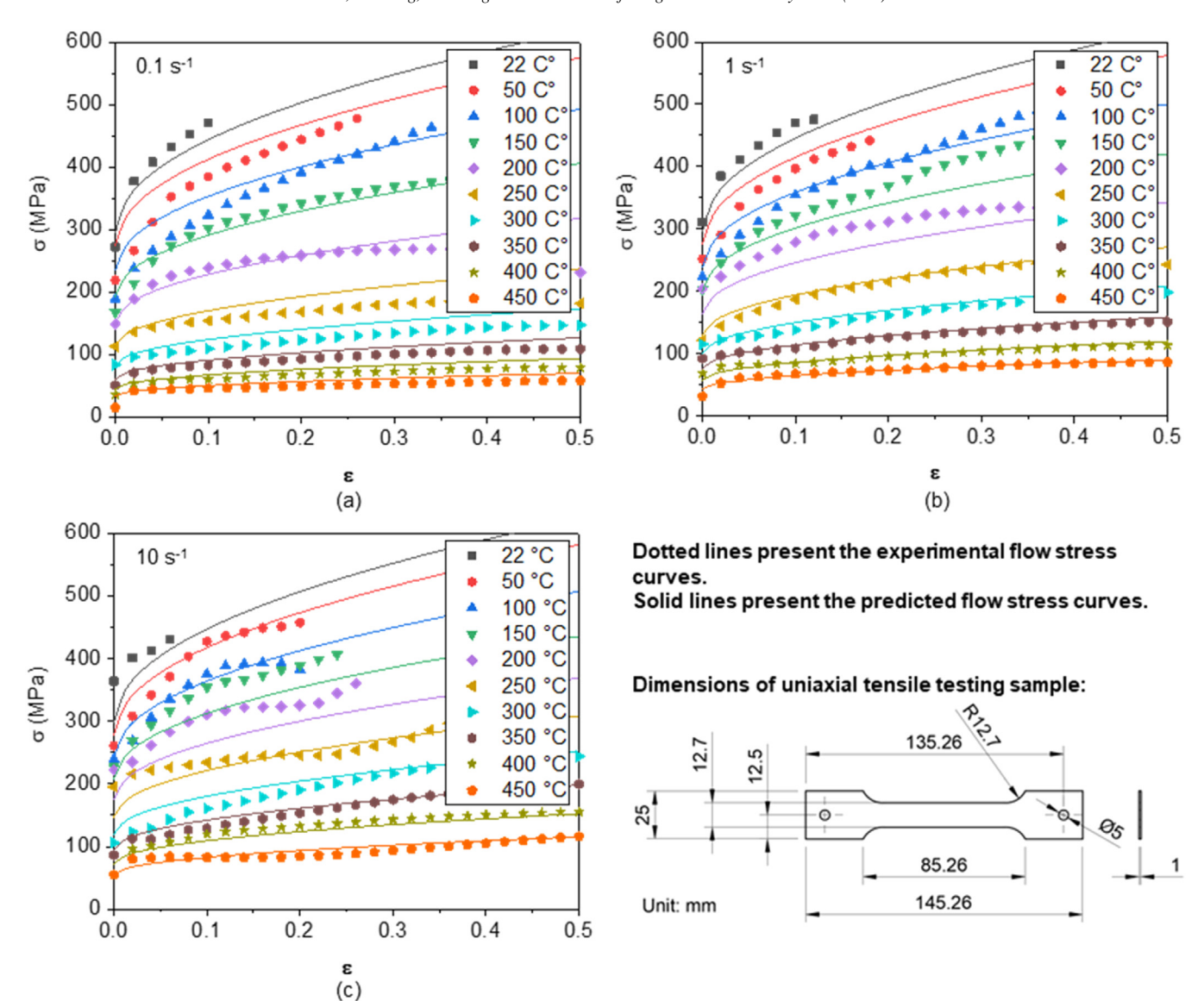


Fig. 6. Experimental and predicted flow stress curves of AZ31B-H24. (a) Strain rate of $0.1~s^{-1}$. (b) Strain rate of $1~s^{-1}$. (c) Strain rate of $10~s^{-1}$.

(FB) model [47], as given below:

10

$$\sigma = (A + B\varepsilon^n)(\dot{\varepsilon}^*)^{\mathcal{C}} \tag{12}$$

$$\dot{\varepsilon}^* = \frac{\dot{\varepsilon}}{\dot{\varepsilon}_0} \tag{13}$$

where σ is the von Mises equivalent stress; ε is the equivalent plastic strain; $\dot{\varepsilon}^*$ is the homologous strain rate; ε and $\dot{\varepsilon}_0$ are the strain rate and reference strain rate, respectively; A is the initial yield strength at reference strain rate and temperature; B is a material constant; n is the strain hardening exponent; C is the strain rate sensitivity exponent. As the strain rate mainly lies in the range of 1 s⁻¹ to 5 s⁻¹ in ISF and the forming starts at room temperature, the strain rate of 1 s⁻¹ and temperature of 22 °C are selected as the reference strain rate and temperature. A is identified as the initial yield strength, while B and n are identified by plotting and fitting the σ - ε curve

at the selected condition as shown in Fig. 7(a). C is identified as the slope by plotting and fitting the $\ln \sigma - \ln \dot{\varepsilon}^*$ curve at a plastic strain of 0.07 as shown in Fig. 7(b). However, the slopes of the $\ln \sigma - \ln \dot{\varepsilon}^*$ curves show an increasing trend with the elevation of temperatures. A new formula is developed to describe and predict the temperature dependency of the strain rate effect as following:

$$C = \frac{C_0}{C_1 + \exp\left(-C_2 T^*\right)} \tag{14}$$

$$T^* = \frac{T - T_0}{T_{\rm m} - T_0} \tag{15}$$

where T^* is the homologous temperature; T, T_0 and T_{melt} are the temperature, reference temperature (room temperature T_{room} in this study) and the melting temperature, respectively; C_0 , C_1 and C_2 are material constants to reflect the temperature dependence of strain rate. From Fig. 7(c) the C values

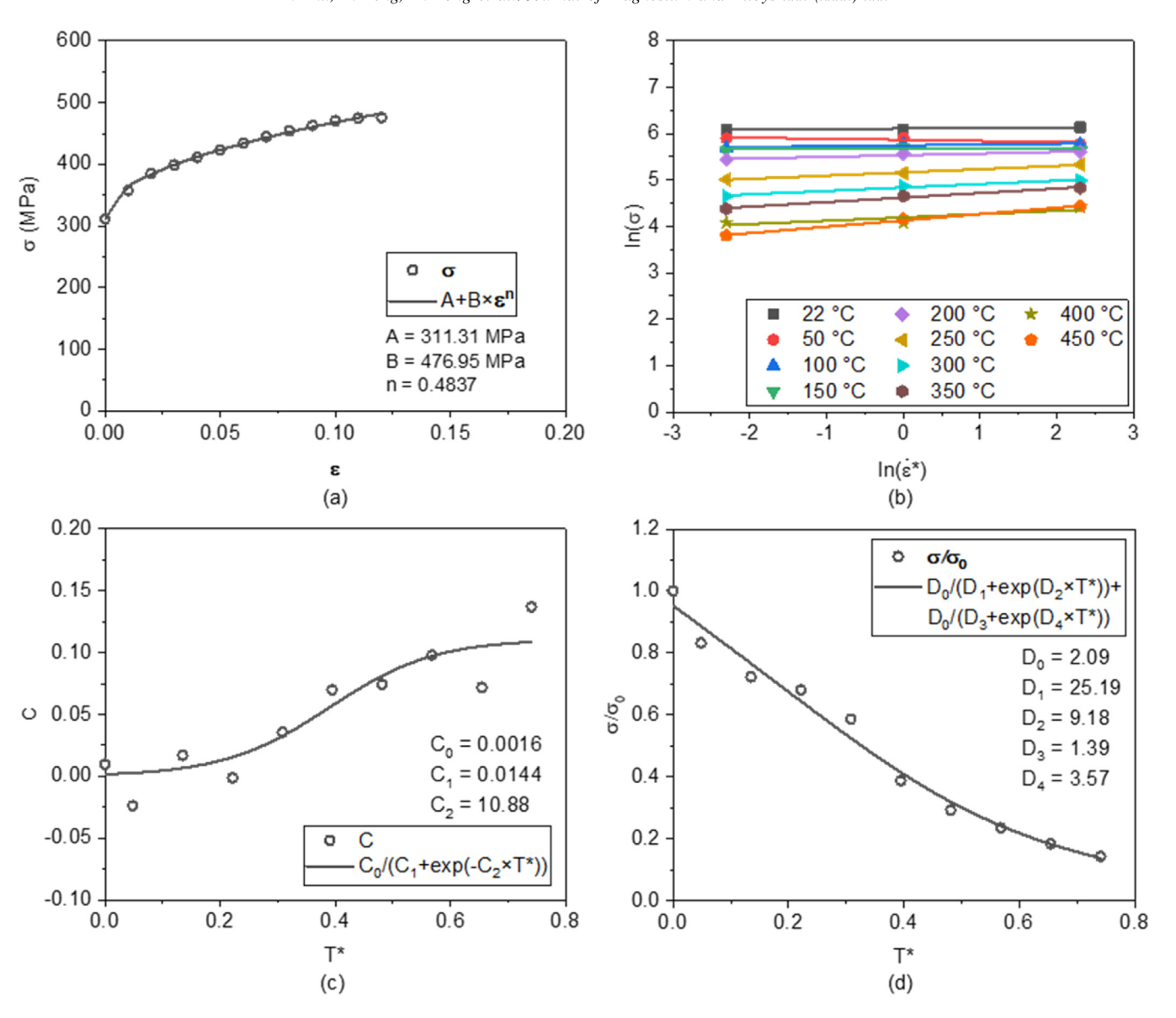


Fig. 7. Parameter identification of the constitutive model of AZ31B-H24 at different temperature and strain rate. (a) Identification of strain effect on the flow stress at the reference temperature and strain rate. (b) Identification of strain rate effect on the flow stress. (c) Identification of the temperature dependence of strain rate effect. (d) Identification of temperature effect on the flow stress.

at different T^* and the fitting result of C_0 , C_1 and C_2 are obtained.

As shown in Fig. 7(d), the flow stress, normalised by the flow stress σ_0 at reference strain rate and temperature, is extracted at the same plastic strain of 0.07, strain rate of 1 s⁻¹ under different temperatures normalised by room temperature. The dependent relationship between the flow stress and the temperature has two different trends below 200 °C and over 250 °C. The complicated temperature dependency is described and predicted by the development of the following formula:

$$\sigma = \sigma_0 \left[\frac{D_0}{D_1 + \exp(D_2 T^*)} + \frac{D_0}{D_3 + \exp(D_4 T^*)} \right]$$
 (16)

where D_0 , D_1 , D_2 , D_3 , D_4 are material constants to reflect the temperature dependence of the flow stress, which are identi-

fied by fitting the formula on the $\frac{\sigma}{\sigma_0} - T^*$ curve as given in Fig. 7(d).

To summarize, the newly developed constitutive model for AZ31B-H24 over the identified range of strain rate and temperature is given as following:

$$\sigma = (A + B\varepsilon^{n}) (\dot{\varepsilon}^{*})^{\frac{C_{0}}{C_{1} + \exp(-C_{2}T^{*})}}$$

$$\left[\frac{D_{0}}{D_{1} + \exp(D_{2}T^{*})} + \frac{D_{0}}{D_{3} + \exp(D_{4}T^{*})} \right]$$
(17)

The parameters for the constitutive model are identified as listed in Table 3. The comparison between the experimental and predicted flow stress curves are presented in Fig. 6. As shown in Fig. 5, the calculated mean strain rate with the ISF feed rate of 1000 mm/min, step size of 0.3 mm, tool diameter of 10 mm and sheet thickness of 1 mm is roughly 1 s^{-1} , while

Table 3 Material parameters of the constitutive model of AZ31B-H24.

A (MPa)	B (MPa)	n	C_0	C_1	C_2	D_0	D_1	D_2	D_3	D_4
311.31	476.95	0.4837	0.0016	0.0144	10.88	2.09	25.19	9.18	1.39	3.57

the measured temperature in Fig. 10(c) and (d) is stabilised at about 200 °C with tool rotational speed of 3000 rpm and about 250 °C with tool rotational speed of 4000 rpm. With strain rate of 1 s⁻¹, the discrepancy of the constitutive modelling results is about 10% at temperature of 200 °C, while it shows very good agreement at temperature of 250 °C. The agreement demonstrates that the developed constitutive model can give accurate fitting and description of the flow stress at different strains, strain rates and temperatures, and the constitutive model can be used to evaluate the thermal softening effect in FS-ISF and RV-ISF of AZ31B-H24.

3.3. Definition of thermal and vibration softening coefficient

The softening in FS-ISF is mainly achieved by thermal effect, while the softening in RV-ISF results from both thermal and vibration effects. In this study, it is proposed that the thermal and vibration effects are quantified by thermal and vibration softening coefficients $K_{\rm T-FS}$, $K_{\rm T-RV}$ and $K_{\rm Vib}$ for FS-ISF and RV-ISF, respectively. The relationship between the vertical forming forces in RV-ISF or FS-ISF and conventional ISF (C-ISF) at room temperature are expressed as follows, respectively:

$$F_{\rm FS} = F_{\rm C} - \Delta F_{\rm T-FS} = F_{\rm C} (1 - K_{\rm T-FS})$$
 (18)

$$F_{RV} = F_{C} - \Delta F_{T-RV} - \Delta F_{Vib} = F_{C} (1 - K_{T-RV} - K_{Vib})$$
 (19)

where $F_{\rm FS}$, $F_{\rm RV}$ and $F_{\rm C}$ are the vertical forming forces in FS-ISF, RV-ISF and C-ISF, respectively. $\Delta F_{\rm T-FS}$, $\Delta F_{\rm T-RV}$ and $\Delta F_{\rm Vib}$ are the vertical forming force reduction due to the thermal and vibration effects in FS-ISF and RV-ISF, respectively.

As revealed by Aerens et al. [48], the vertical forming force F in ISF has linear relationship with the mean material equivalent stress $\sigma_{\rm m}$ as following:

$$F \propto \sigma_{\rm m}$$
 (20)

$$\Delta F \propto \Delta \sigma_{\rm m}$$
 (21)

where ΔF and $\Delta \sigma_{\rm m}$ are the reduction in vertical forming force and the mean equivalent stress.

As illustrated in Fig. 8, the thermal softening effect due to temperature increases leads to the flow stress reduction in heated uniaxial tension condition and the forming force reduction in FS-ISF condition, where localised temperature elevation is generated by friction heating. While the vibration softening effect may also lead to the additional tensile stress reduction in heated and vibrated uniaxial tension condition and the additional forming force reduction in RV-ISF,

where localised vibration of the sheet is generated by periodical loses of the contact in addition to the friction heating effect. Therefore, the following relationships of the vertical force reduction can be proposed for FS-ISF and RV-ISF conditions, respectively:

$$\Delta F_{\text{T-FS}} \propto \Delta \sigma_{\text{T}}$$
 (22)

$$\Delta F_{\text{T-RV}} \propto \Delta \sigma_{\text{T}}$$
 (23)

$$\Delta F_{\rm RV} \propto \Delta \sigma_{\rm Vib}$$
 (24)

where $\Delta\sigma_T$ is the tensile stress reduction due to thermal effect and $\Delta\sigma_{Vib}$ is the tensile stress reduction due to vibration effect.

3.4. Determination of thermal softening coefficient

According to the developed constitutive model, given the same plastic strains and strain rates, the equivalent stress $\sigma_{\rm T-FS}$ and $\sigma_{\rm T-RV}$ at elevated temperatures $T_{\rm FS}$ and $T_{\rm RV}$ recorded in the FS-ISF and RV-ISF tests can be calculated by Eq. (17).

In the FS-ISF, the vertical forming force reduction ΔF_{T-FS} only results from the thermal effect at elevated temperatures T_{FS} , and this can be easily obtained as following:

$$\Delta F_{\text{T-FS}} = F_{\text{C}} - F_{\text{FS}} \tag{25}$$

where $F_{\rm C}$ can be measured by C-ISF at room temperature, but for AZ31B-H24 in this study, this cannot be obtained experimentally because of early fracture due to the material brittleness at room temperature. However, based on the linear relationship shown in Eq. (20), the theoretical $F_{\rm C}$ can be calculated by the vertical forming force $F_{\rm FS3000}$ and the flow stress $\sigma_{\rm T-FS3000}$ at the recorded temperatures in the FS-ISF condition with the tool rotational speed of 3000 rpm, and the theoretical flow stress $\sigma_{\rm room}$ at room temperature in C-ISF condition, using the following formula according to Eq. (20):

$$F_{\rm C} = F_{\rm FS3000} \frac{\sigma_{\rm room}}{\sigma_{\rm T-FS3000}} \tag{26}$$

In RV-ISF however, both thermal and vibration effects exist, so the force reduction $\Delta F_{\rm T-RV}$ due to thermal effect only cannot be easily calculated by the force measurement. By considering the temperature difference between FS-ISF and RV-ISF under the same tool rotational speed, the force reduction $\Delta F_{\rm T-RV}$ due to thermal effect in RV-ISF can be calculated as following by the force reduction in FS-ISF and the additional theoretical force difference $\Delta F_{\rm T-FS-RV}$ due to the

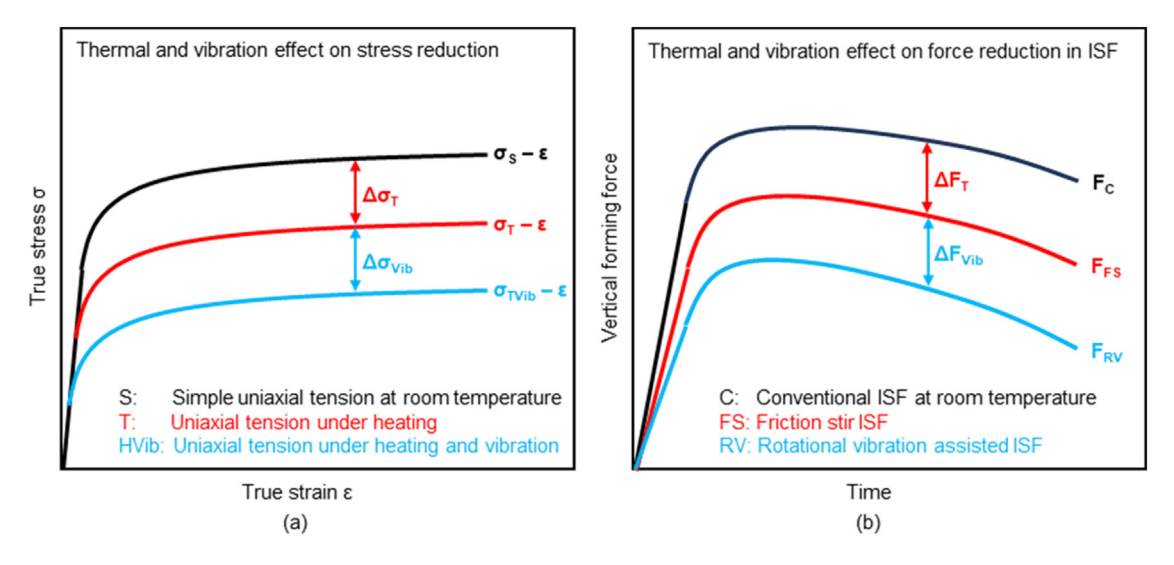


Fig. 8. Illustration of thermal and vibration softening. (a) Effects on stress reduction in the uniaxial tension condition. (b) Effects on vertical forming force reduction in FS-ISF and RV-ISF.

temperature difference between FS-ISF and RV-ISF with the same rotational speed:

$$\Delta F_{\text{T-RV}} = F_{\text{C}} - F_{\text{FS}} - \Delta F_{\text{T-FS-RV}} \tag{27}$$

 $\Delta F_{\rm T-FS-RV}$ is related to the difference in flow stress reduction due to the temperature difference according to the linear relationship between the vertical forming force and flow stress (Eq. (20)) as given following:

$$\Delta F_{\text{T-FS-RV}} = F_{\text{FS3000}} \frac{\sigma_{\text{T-RV}} - \sigma_{\text{T-FS}}}{\sigma_{\text{FS3000}}}$$
(28)

where σ_{T-FS} and σ_{T-RV} are the theoretical flow stress at the temperature recorded in FS-ISF and RV-ISF, respectively. The thermal softening coefficients K_{T-FS} and K_{T-RV} of FS-ISF and RV-ISF can be obtained as follows:

$$K_{\text{T-FS}} = \frac{\Delta F_{\text{T-FS}}}{F_{\text{C}}} = 1 - \frac{F_{\text{FS}}}{F_{\text{FS3000}}} \frac{\sigma_{\text{T-FS3000}}}{\sigma_{\text{room}}}$$
 (29)

$$K_{\text{T-RV}} = \frac{\Delta F_{\text{T-RV}}}{F_{\text{C}}} = 1 - \frac{F_{\text{FS}}}{F_{\text{FS3000}}} \frac{\sigma_{\text{T-FS3000}}}{\sigma_{\text{room}}} - \frac{\sigma_{\text{T-RV}} - \sigma_{\text{T-FS}}}{\sigma_{\text{room}}}$$
(30)

3.5. Determination of vibration softening coefficient

Unlike the considerable investigation of the constitutive response and modelling of thermal softening effect, the stress reduction due to vibration softening effect and the constitutive modelling are still very limited. In RV-ISF, the vertical forming force reduction due to vibration softening effect can be evaluated by excluding the force reduction due to thermal effect as following:

$$\Delta F_{\text{Vib}} = F_{\text{C}} - F_{\text{RV}} - \Delta F_{\text{T-RV}} = F_{\text{FS}} - F_{\text{RV}} + \Delta F_{\text{T-FS-RV}}$$
(31)

The vibration softening coefficient K_{Vib} is calculated as following:

$$K_{\text{Vib}} = \frac{\Delta F_{\text{Vib}}}{F_{\text{C}}} = \frac{F_{\text{FS}} - F_{\text{RV}}}{F_{\text{FS3000}}} \frac{\sigma_{\text{T-FS3000}}}{\sigma_{\text{room}}} + \frac{\sigma_{\text{T-RV}} - \sigma_{\text{T-FS}}}{\sigma_{\text{room}}}$$
 (32)

4. Results

4.1. Forming force and temperature variation

Fig. 9 shows the variation of the vertical forming force and temperature in FS-ISF and RV-ISF using different tools and different spindle speeds. The evolution of vertical forming force can be divided into increasing and decreasing stages, while the temperature evolution can be divided into increasing and stabilised stages. Compared to the early stage of FS-ISF and RV-ISF process, due to the increased contact area and strain hardening of the flow stress, and more sheet material involved in the localised deformation in the later stage of the process, it leads to the increasing stage of the vertical forming force. With the increase of the drawing angle, the sheet thickness under contact is reduced, and most importantly, the forming temperature increases and stabilizes on an elevated level after accumulated temperature reaches a state when heat gain and heat loss are in balance. Besides, the use of T2 and T3 in RV-ISF also results in additional force reduction, due to vibration effect, as compared with FS-ISF using T0. These cause the decrease of the vertical forming force after the increasing stage. With the use of different tools and tool rotational speeds, time required to reach the decreasing stage of the vertical forming force varies. FS-ISF using T0 has the longest reaching time to the decreasing stage followed by RV-ISF using T3, while RV-ISF using T2 has the earliest reaching time. For all the three tools, the increase of tool rotational speed leads to the earlier reach to decreasing stage of the vertical forming force as well as the stabilised

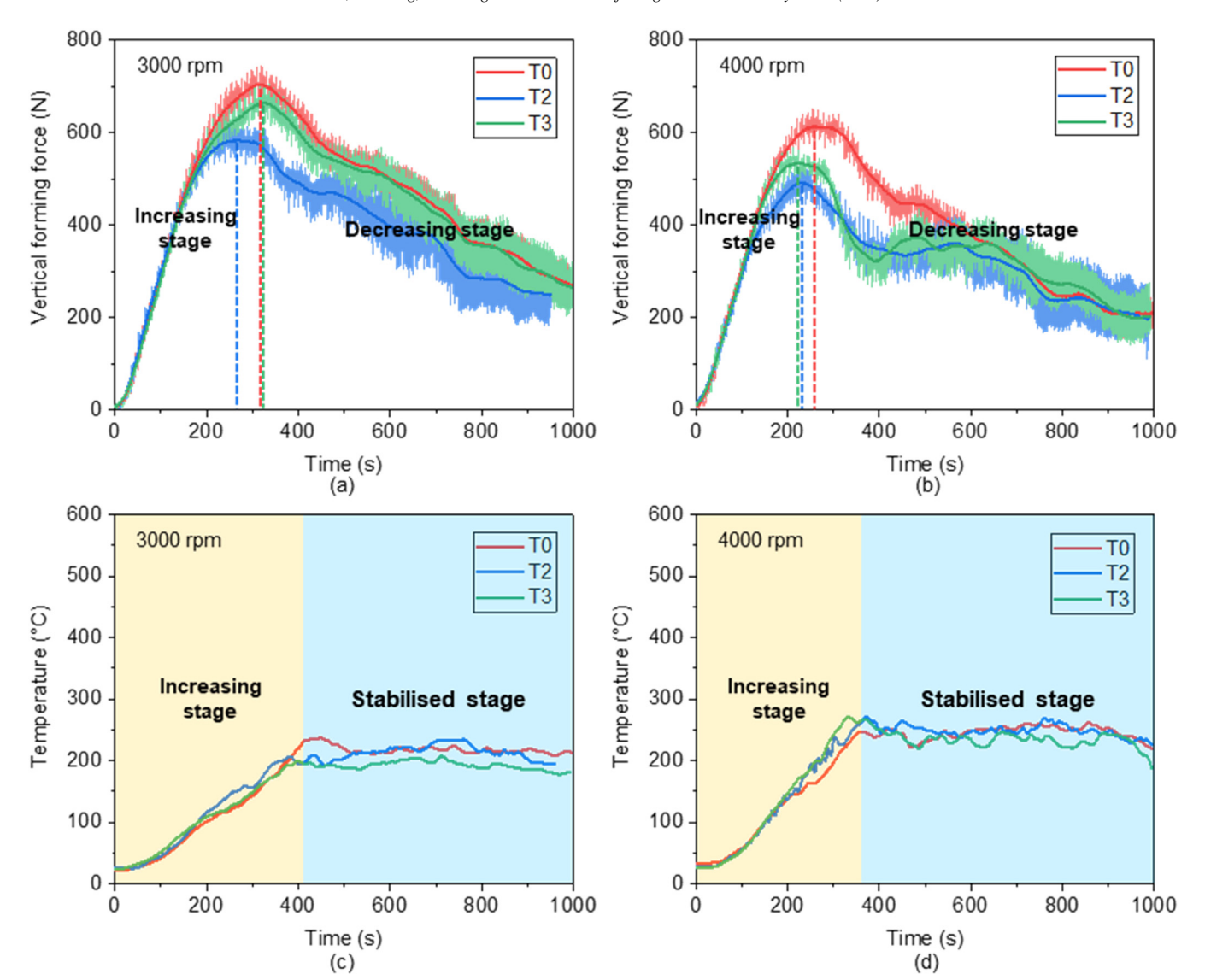


Fig. 9. Vertical forming force and temperature history in FS-ISF and RV-ISF of AZ31B-H24 sheets. (a) Vertical forming forces with 3000 rpm. (b) Vertical forming forces with 4000 rpm. (c) Temperature evolution with 3000 rpm. (d) Temperature evolution with 4000 rpm.

stage of forming temperature. The increase of the tool rotational speed increases the forming temperature thus reduces the vertical forming force. RV-ISF using T2 has a similar temperature level with FS-ISF using T0 at the same rotational speeds, while RV-ISF using T3 has about 10% lower temperature than RV-ISF using T0 due to the reduction of the tool-sheet contact area. However, the vertical forming force in RV-ISF using T2 shows obvious drop from FS-ISF using T0 with similar forming temperature, especially 17% lower from the peak force, while that of T3 also shows slight reduction trend with about 6% lower from the peak force although the temperature in RV-ISF with T3 is lower, indicating vibration effect on force reduction.

4.2. Force reduction from FS-ISF to RV-ISF

14

Fig. 10 shows the calculation results of the reduction values of the vertical forming force and the reduction rates from FS-ISF using T0 to RV-ISF using T2 and T3 with the same tool rotational speeds. For both rotational speeds of 3000 rpm and 4000 rpm, the force reduction achieved by T3 is less significant than that by T2. The first explanation for this observation is that the reduced contact area of T3 in a single rotation of the tool due to cutting the grooves on the surface leads to the less friction heat accumulation. The second explanation is that the vibration amplitude by T3 is smaller than that produced by T2 although its vibration frequency is higher because of more impacts generated by each tool rotation of T3, as listed in Table 2. With a rotational speed of 4000 rpm, the reduction values and rates show different trends, different from what is observed in RV-ISF with 3000 rpm. The limitation of the direct calculation and comparison of the force reduction values and the rates from FS-ISF to RV-ISF is the difficulty to decoupling the thermal and vibration effects and less clear relevance to the variation trends at different rotational speeds.

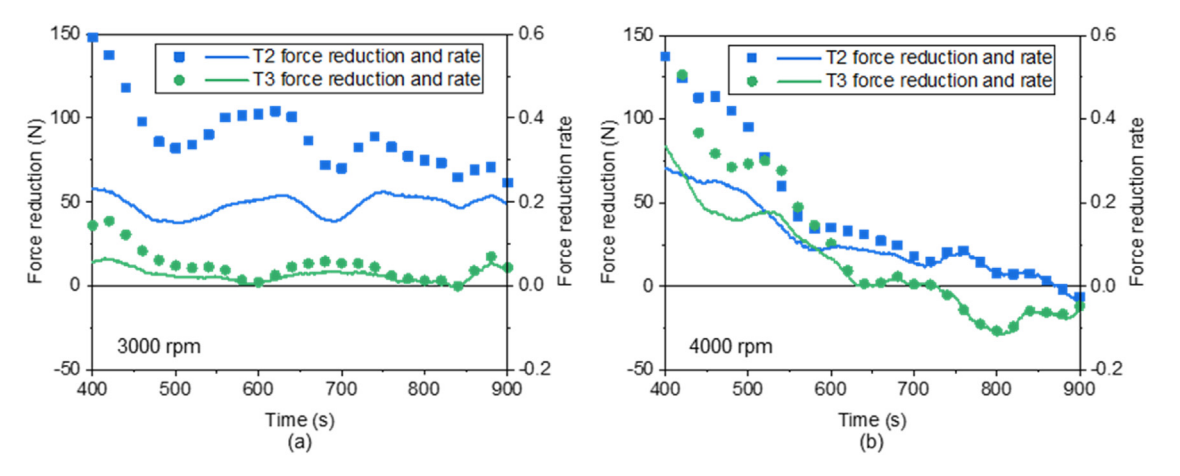


Fig. 10. Force reduction and reduction rate from FS-ISF to RV-ISF by using T2 and T3 tools. (a) With the same tool rotational speed of 3000 rpm. (b) With the same tool rotational speed of 4000 rpm.

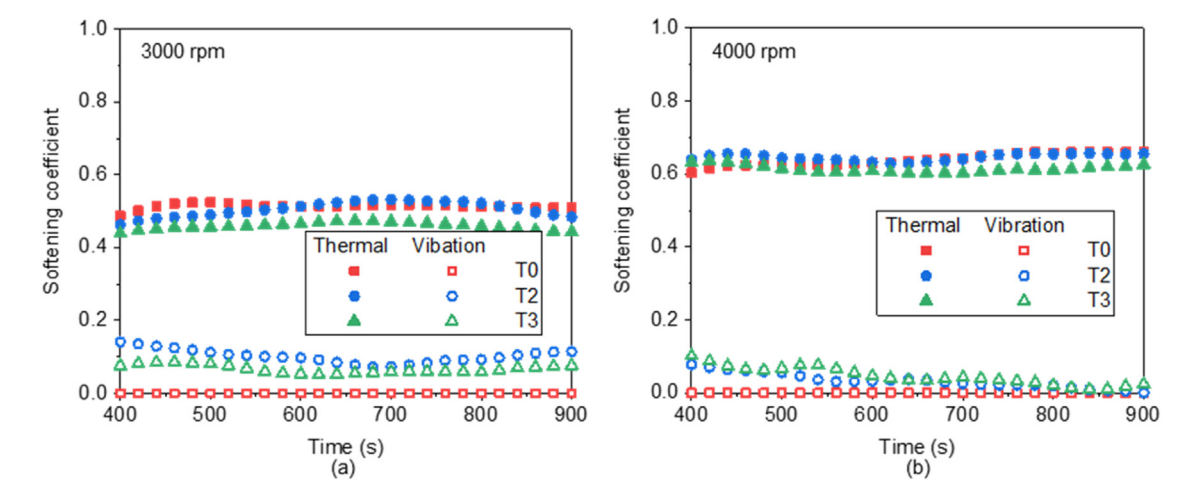


Fig. 11. Effect of different tool designs on the thermal and vibration softening coefficients in FS-ISF and RV-ISF. (a) With the same tool rotational speed of 3000 rpm. (b) With the same tool rotational speed of 4000 rpm.

4.3. Thermal and vibration softening in FS-ISF and RV-ISF

Fig. 11 shows the softening coefficients of thermal and vibration effects in FS-ISF and RV-ISF of AZ31B-H24. The thermal effect takes a main role in the softening behaviour with a softening coefficient of 45~65% and the thermal softening coefficient rises with the increase of the tool rotational speed. By comparing the softening coefficients using different tools at the same tool rotational speed, the tool T0 produces the most thermal softening, while the tool T3 produces the least. The difference becomes smaller with the increase of the tool rotational speed. Without vibration generation in FS-ISF using T0, the vibration softening coefficient is shown to be 0. However, for the RV-ISF using T2 and T3 with tool rotational speed of 3000 rpm, the vibration softening coefficients are calculated as around 15% and 10%, respectively, which means that the vibration only causes 15% and 10% of the vertical forming force reduction from C-ISF at room temperature. T2 and T3 produce less vibration softening when 4000 rpm is applied but have the similar vibration softening effects. This shows the reduced vibration effect at higher temperatures with higher tool rotational speed of 4000 rpm.

4.4. Grain distribution

Fig. 12 presents the grain distribution, texture, deformed grains, recrystallised grains, relative frequency of deformed grain boundary disorientation angle and Kernel average misorientation (KAM) distribution of the as-received AZ31B-H24. The texture exhibits a typical rolling texture, characterised by a basal pole split along the ND (0001//ND) of the sheet thickness [49]. The raw material has the initial average grain size of 44.15 μm^2 , recrystallisation degree of 26.4%, LAGBs fraction of 58.6% in deformed grains and geometrically necessary dislocation (GND) density of $2.18\times10^{14}~\text{m}^{-2}$ calculated from the mean KAM. The details of the identification of recrystallisation degree, LAGBs in deformed grains and GND density are given in Sections 4.5, 4.6 and 4.7, respectively.

Fig. 13 shows the grain distribution of AZ31B-H24 with 50% thickness reduction after FS-ISF by T0 and RV-ISF by T3 with the tool rotational speed of 3000 rpm, respectively. As compared in Fig. 14(a), both FS-ISF using T0 and RV-ISF using T3 significantly reduced the average grain size from 44.15 μm in the as-received material, while the av-

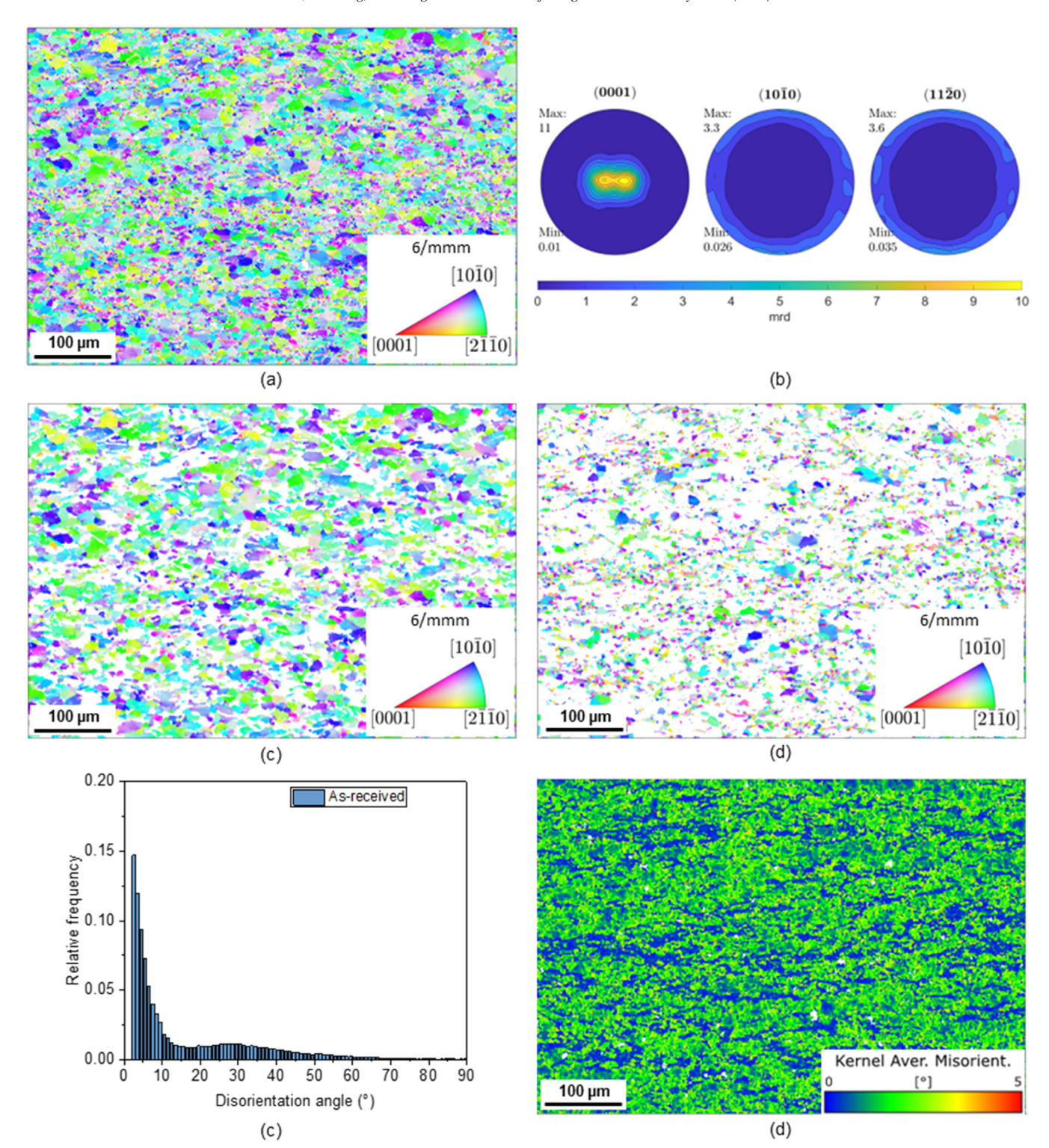


Fig. 12. Microstructure of as-received AZ31B-H24 sheet. (a) Inverse pole figure showing the grain distribution. (2) Pole figures showing the texture. (c) Deformed grains. (d) Recrystallised grains. (e) Relative frequency of deformed grain boundary disorientation angle. (f) KAM distribution with scanning step size of 1 μm.

erage grain size produced by RV-ISF using T3 (0.94 μ m, 2.3 μ m and 2.19 μ m in the top, middle and bottom layers, respectively) is smaller than that produced by FS-ISF using T0 (1.06 μ m, 2.63 μ m and 2.7 μ m in the top, middle and bottom layers, respectively). It is noteworthy that

16

the large standard deviations of the grain sizes in Fig. 14(a) result from the coexistence of small and large grains. For both tested samples, a thin layer of refined grains is observed on the top surface of the sheet contacting the forming tool, as shown in Fig. 13(a) and (b), while less-refined

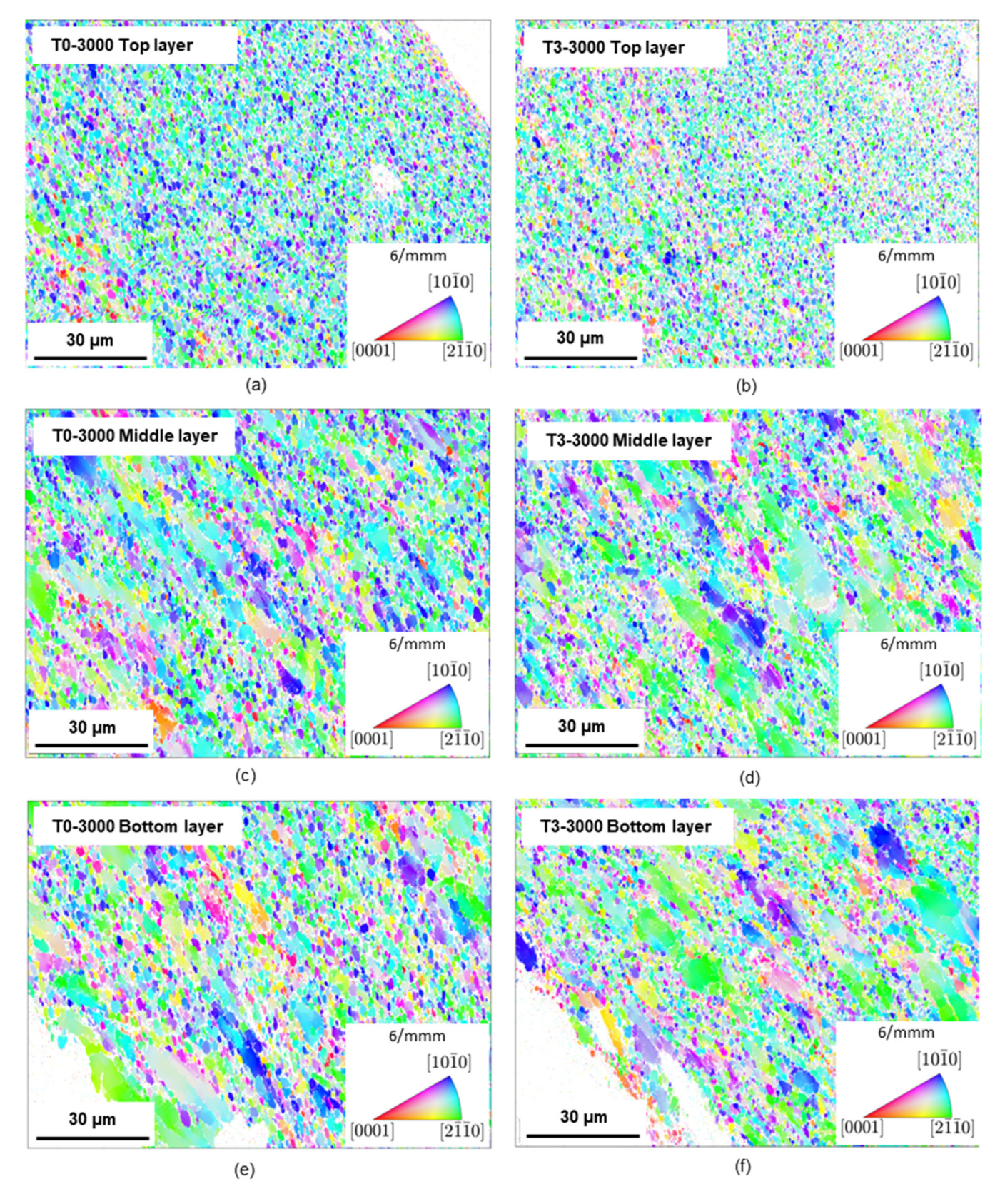


Fig. 13. Grain distribution after FS-ISF and RV-ISF. (a), (c), (e) Top, middle, bottom layer of the sheet deformed by T0-3000. (b), (d), (f) Top, middle, bottom layer of the sheet deformed by T3-3000.

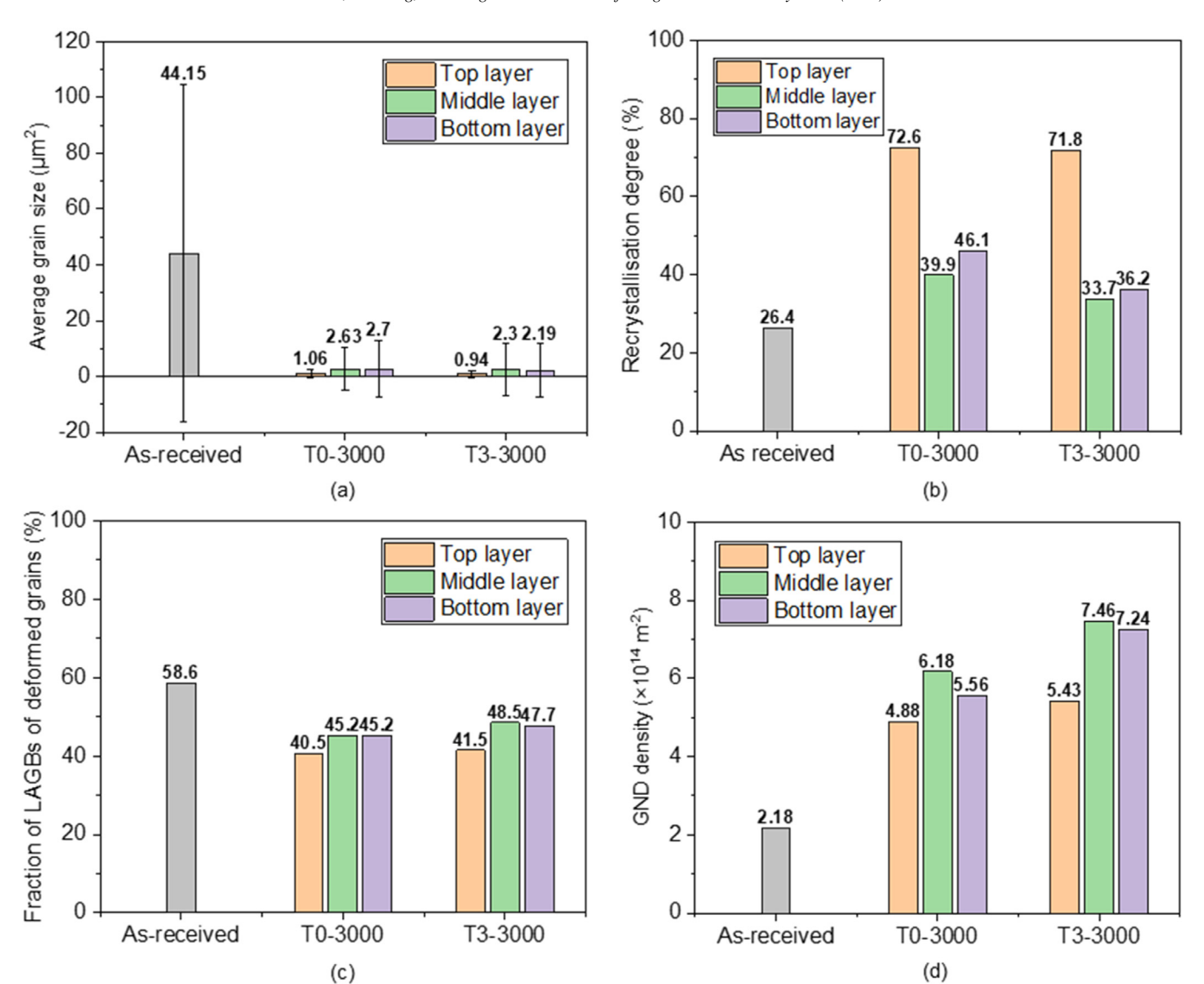


Fig. 14. Comparison of the microstructure as received with that after FS-ISF (T0-3000) and RV-ISF (T3-3000). (a) Average grain size. (b) Recrystallisation degree. (c) Fraction of LAGBs of deformed grains. (d) GND density.

grains are observed in the rest of the thickness of the samples.

4.5. Recrystallisation degree

18

Using the grain orientation spread (GOS) criterion, the textures of deformed and recrystallised grains are analysed after separation. Recrystallised grains are identified by a GOS of less than 3°, while grains with a GOS of 3° or higher are categorised as deformed [50]. Fig. 15 illustrates that the deformed grains by T3 with 3000 rpm exhibit a significantly stronger texture intensity compared to the recrystallised grains, particularly in the 0001//ND alignment. The prismatic poles in the deformed grains align well, with 10–10//RD and 11–20//TD, showing similar intensities around 4.7–4.8. In contrast, the recrystallised grains show a significant decrease in prismatic alignment intensity, with a slight tilt of the 11–20 poles from TD toward RD. The morphological features further corrobo-

rate the separation of deformed and recrystallised grains. Deformed grains are elongated and irregular, reflecting strain-induced deformation, while recrystallised grains exhibit an equiaxed morphology, an indication of dynamic recrystallisation. These findings demonstrate the effectiveness of the GOS criterion in distinguishing deformed and recrystallised grains and confirm that recrystallisation has occurred during the ISF process.

The recrystallisation degree is reflected by the area fraction of recrystallised grains. As shown in Figs. 16 and 14(b), with 3000 rpm, the recrystallisation degree is reduced by RV-ISF using T3 (71.8%, 33.7% and 36.2% in the top, middle and bottom layers, respectively) and FS-ISF using T0 (72.6%, 39.9% and 46.1% in the top, middle and bottom layers, respectively) as compared to the as-received state (26.4%). A higher recrystallisation degree is observed on the top layer of the sheet surface contacting the forming tool than that on the rest material through the thickness. This indicates that the

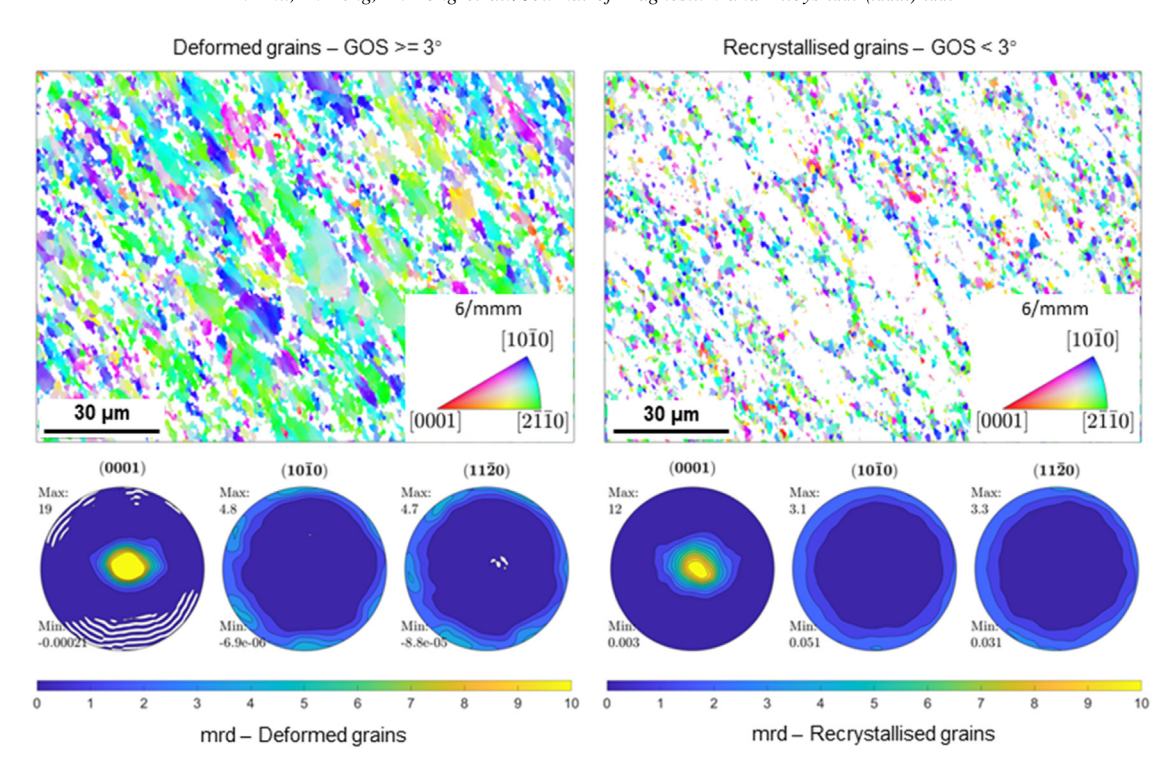


Fig. 15. Deformed grains (GOS \geq 3°) and recrystallised grains (GOS < 3°) of T3-3000 with pole figures.

large shear deformation of the sheet surface and temperature rise dominate the recrystallisation process.

4.6. Low-angle grain boundary

The grain boundaries with a misorientation angle less than 10° are identified as LAGBs, while the others are identified as high-angle grain boundaries (HAGBs). Fig. 17 presents the LAGBs in the deformed grains, Fig. 18 shows the relative frequency of grain boundary misorientation angle, and Fig. 14(c) gives the fraction of LAGBs after FS-ISF and RV-ISF. From Figs. 17, 18 and 14(c), the observations indicate that with 3000 rpm, the as-received material has the highest fraction of LAGBs in deformed grains, while RV-ISF by T3 produced slightly more LAGBs in deformed grains (41.5%, 48.5% and 47.4% in the top, middle and bottom layers, respectively) than FS-ISF by T0 (40.5%, 45.2% and 45.2% in the top, middle and bottom layers, respectively).

4.7. GND density

Fig. 19 presents the KAM distribution with 50% thickness reduction after FS-ISF by T0 and RV-ISF by T3 with 3000 rpm, respectively. With the KAM distribution, the GND density ρ can be calculated from the mean KAM as following [39,51]:

$$\rho = \frac{\gamma \,\vartheta}{ub} \tag{33}$$

where, γ is a constant which correlates with the geometry of the boundaries ($\gamma = 3$ for the mixed boundaries), θ is

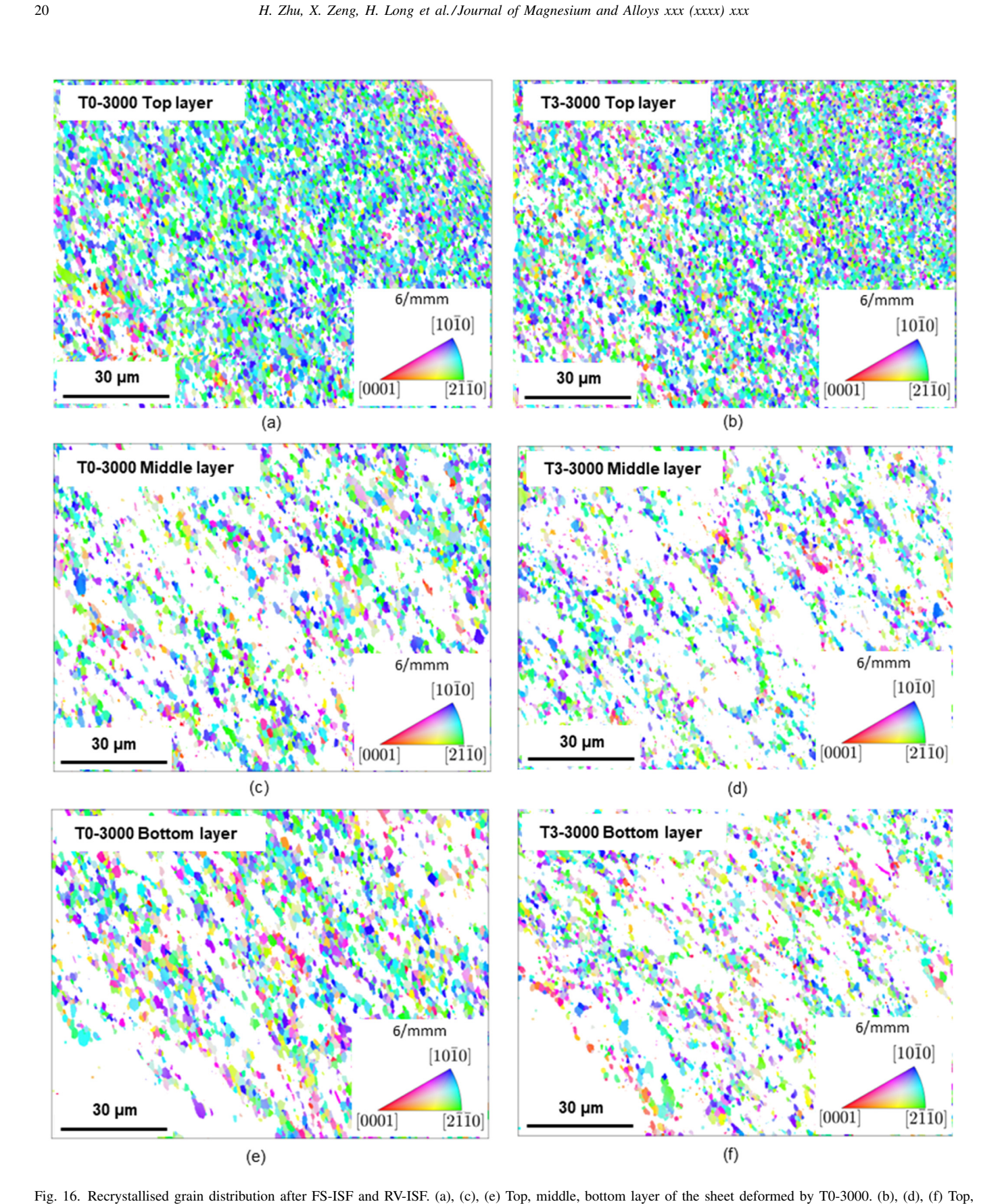
the mean KAM in radians, u is the EBSD step size, and b is the magnitude of the Burgers vector ($b=0.322\,\mathrm{nm}$ for magnesium). Fig. 14(d) shows the comparison of the calculated GND density between as-received material, samples after FS-ISF by T0 and RV-ISF by T3 with 3000. It can be observed that both FS-ISF by T0 and RV-ISF by T3 can increase the GND density as compared to the as-received AZ31B-H24 sheet because of the plastic deformation, while RV-ISF leads to higher GND density as 4.88×10^{14} , 6.18×10^{14} and $5.56 \times 10^{14}\,\mathrm{m}^{-2}$ in the top, middle and bottom layers, respectively, higher than that by FS-ISF.

5. Discussions

5.1. Combined thermal and vibration softening mechanisms

As presented in Section 4.1–4.3, in FS-ISF, only elevated temperatures from friction heat contributes to the softening effect, while in RV-ISF, in addition to the thermal effect, localised vibration is the other effect that the new tool design brings to the deformation process. Although a quantitative connection between the calculated softening contribution and the microstructure investigation is difficult to establish because the decoupling is phenomenological based calculation while the microstructure investigation is physically based, the softening mechanism of combined thermal and vibration effects can be revealed based on the microstructure observations in Section 4.4–4.7.

It is well acknowledged that the mechanism of the thermal softening effect in magnesium alloys is the activation of additional slip systems, recovery and recrystallisation. The



middle, bottom layer of the sheet deformed by T3-3000.

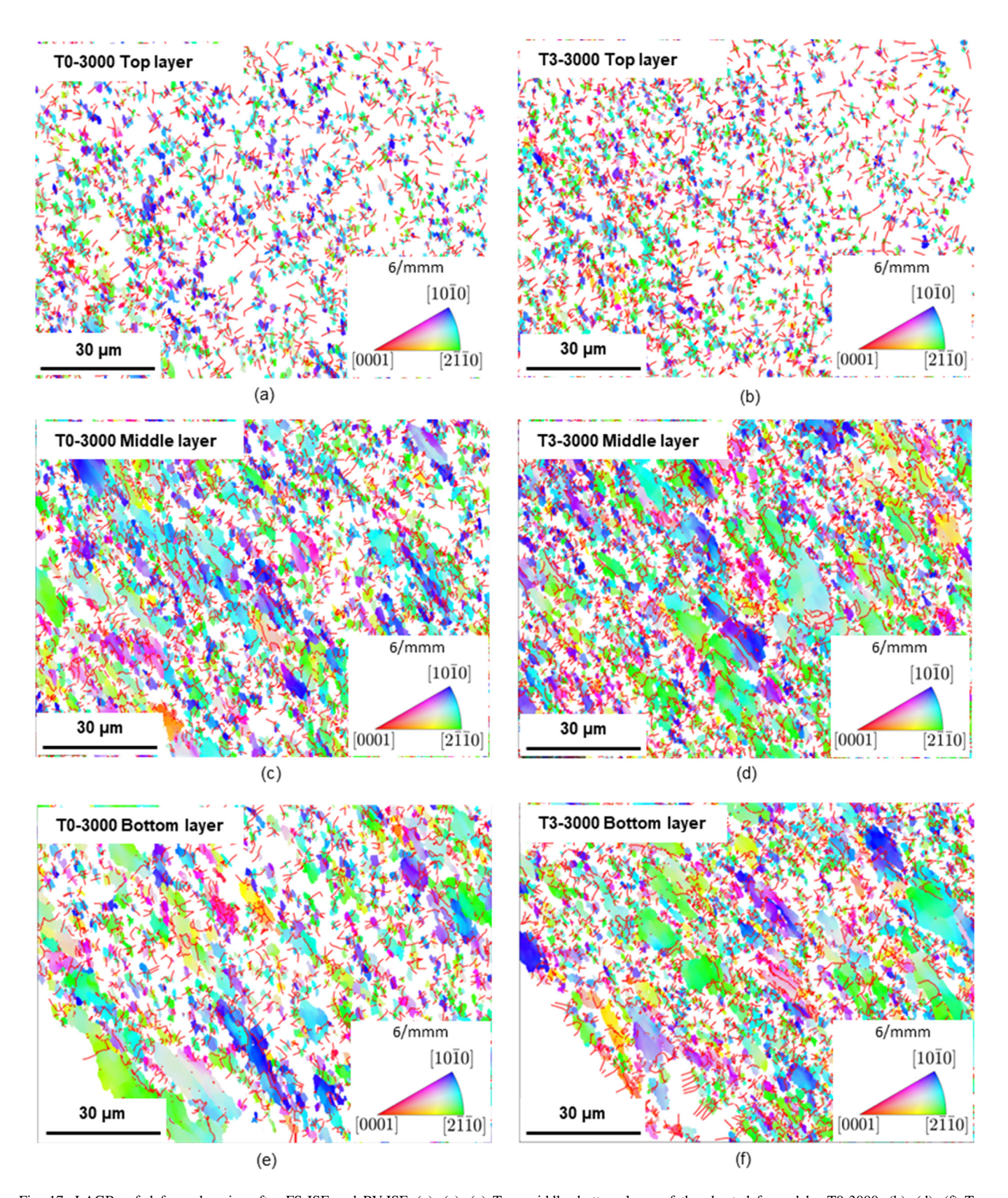


Fig. 17. LAGBs of deformed grains after FS-ISF and RV-ISF. (a), (c), (e) Top, middle, bottom layer of the sheet deformed by T0-3000. (b), (d), (f) Top, middle, bottom layer of the sheet deformed by T3-3000.

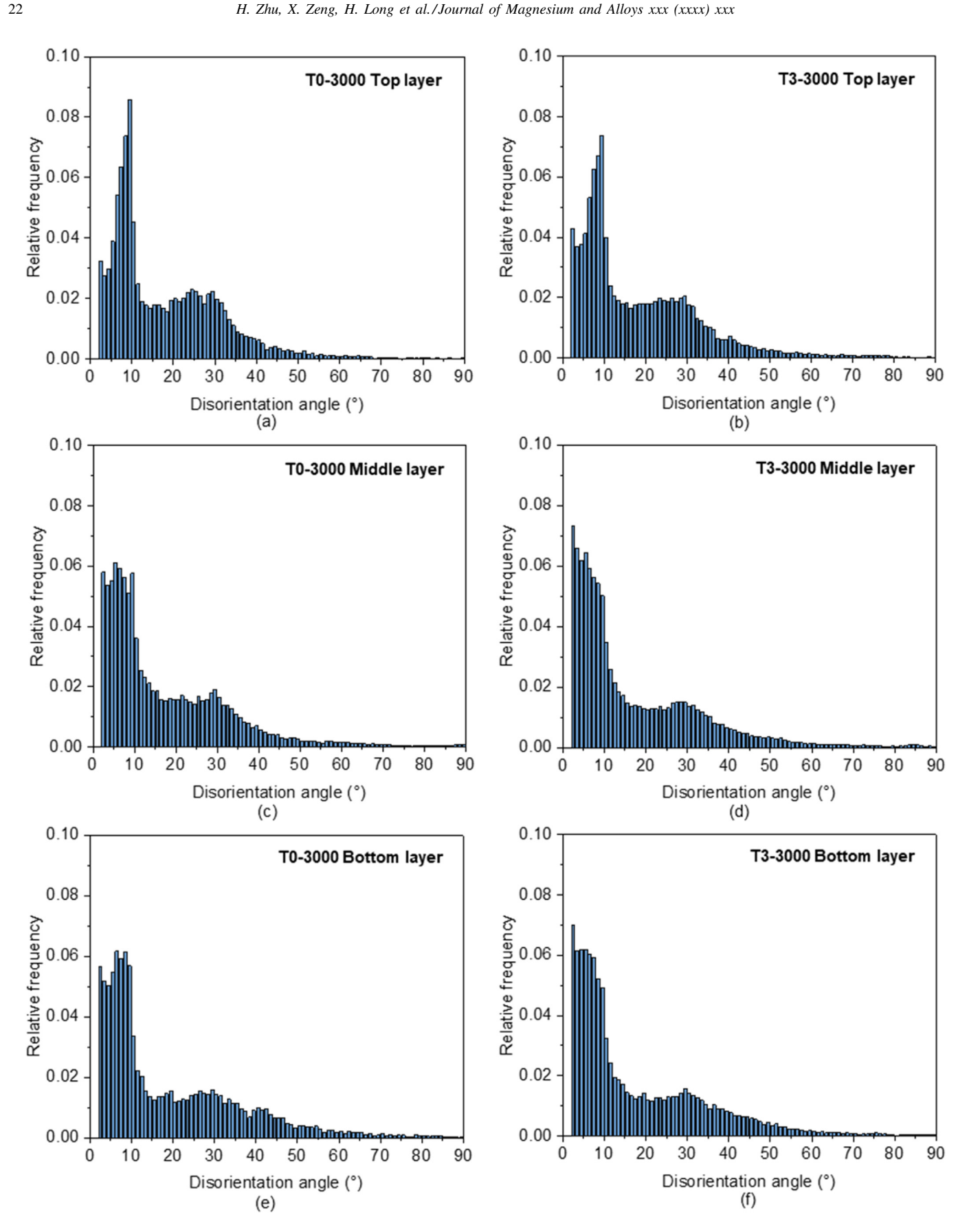


Fig. 18. Relative frequency of deformed grain boundary disorientation angle after FS-ISF and RV-ISF. (a), (c), (e) Top, middle, bottom layer of the sheet deformed by T0-3000. (b), (d), (f) Top, middle, bottom layer of the sheet deformed by T3-3000.

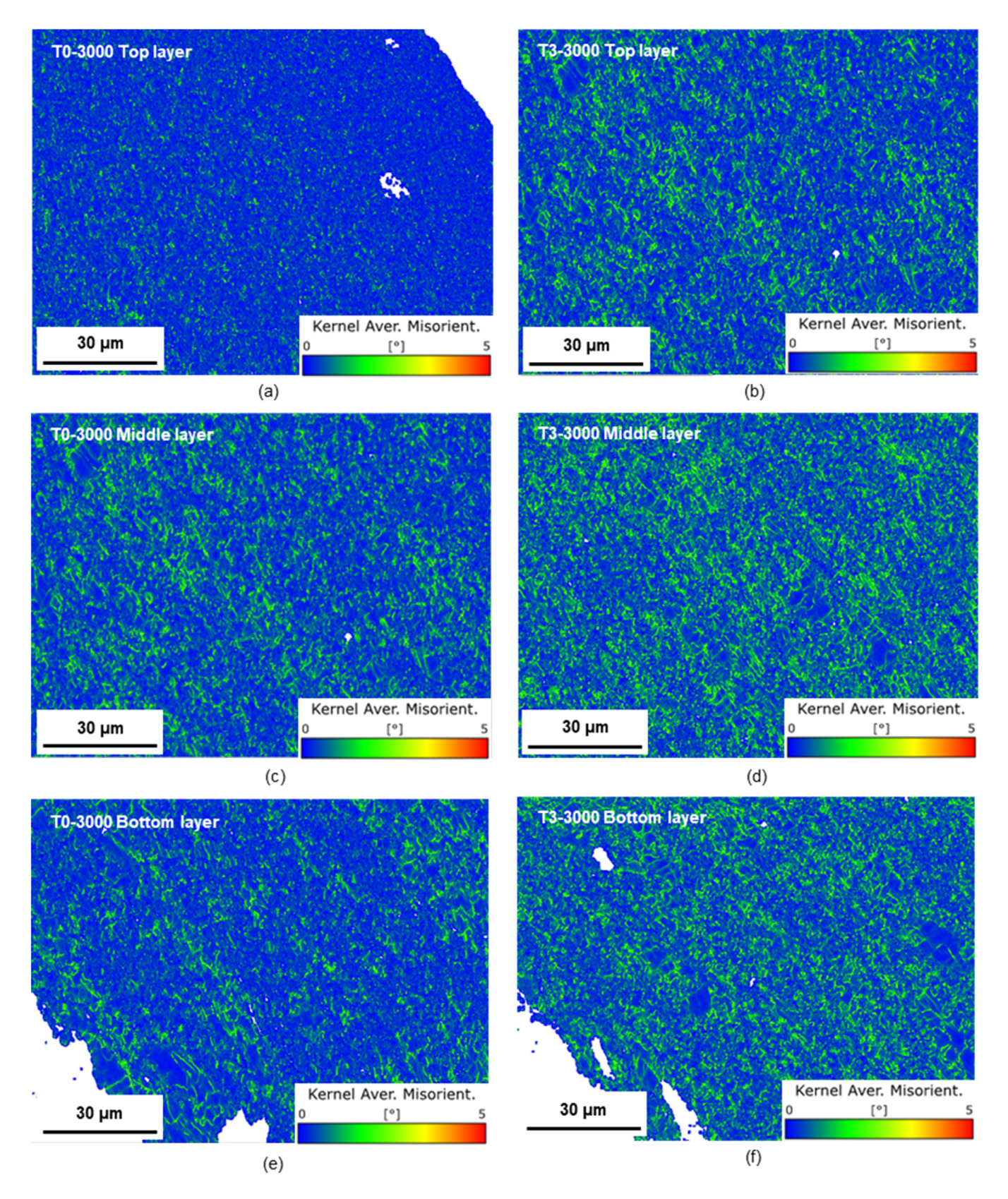


Fig. 19. KAM after FS-ISF and RV-ISF. (a) Top layer by T0-3000 (scanning step size of 0.13 μ m). (b) Top layer by T3-3000 (scanning step size of 0.15 μ m). (c) Middle layer by T0-3000 (scanning step size of 0.15 μ m). (d) Middle layer by T3-3000 (scanning step size of 0.15 μ m). (e) Bottom layer by T0-3000 (scanning step size of 0.15 μ m). (f) Bottom layer by T3-3000 (scanning step size of 0.15 μ m).

localised contact area of sheet material undergoes repeated plastic deformation several times while the tool moving pass over the contact area, depending on the forming geometry and toolpath design. Both dynamic and static recovery and recrystallisation exist in the intermittent contact and deformation process. During the loading state under the tool-sheet localised contact, the enhanced activation of slip systems, dynamic recovery and recrystallisation happen simultaneously to reduce the work hardening and lead to material softening. However, during the unloading state without being in contact with the tool, static recovery and recrystallisation continue softening the sheet material without the occurrence of work hardening.

Different from the well-studied mechanism of thermal softening effect, the mechanism of vibration softening is understudied and less understood, making it difficult to explain the force reduction in RV-ISF.

As observed in Section 4.5, the RV-ISF using T3 with 3000 rpm can reduce the recrystallisation degree in the deformed AZ31B-H24. With the same material and processing time, the key factors for the recrystallisation are the stored energy and the temperature. Although higher GND density is produced by RV-ISF (T3-3000), the forming temperature is actually lower than that in FS-ISF (T0-3000). Subsequently, there may be two reasons for the reduced recrystallisation degree: one is the temperature decrease from FS-ISF to RV-ISF due to the reduced contact area, while the other is due to the local vibration effect in RV-ISF but absent in FS-ISF.

As investigated in Section 4.7, with the tool rotational speed of 3000 rpm, the sample produced by RV-ISF of AZ31B-H24 results in the increased GND density as compared to the sample produced by FS-ISF. Both the introduction of localised vibration effect and the lower temperature in RV-ISF, as shown in Figs. 9(c), can result in less dislocations involved into the grain boundary migration in recrystallisation and thus higher dislocation density.

LAGBs form when dislocations rearrange into ordered, low-energy configurations. During this rearrangement, dislocations of opposite signs may come into contact and annihilate each other. This reduces the net dislocation density and further decreases the stored energy. The remaining dislocations form a coherent structure that defines a LAGB. This means that the formation of LAGBs can reflect the activity of dislocation rearrangement and annihilation. At lower temperature in RV-ISF with T3 as compared with FS-ISF with T0, the recovery is less active, so dislocation annihilation and rearrangement into ordered configurations are suppressed. Consequently, the dislocation density remains higher, but fewer dislocations can organise into stable LAGBs to be detected by EBSD. This should have led to a reduced LAGB fraction in the deformed grains, even though the stored energy associated with dislocations is greater. However, as observed in Section 4.6, an increase of the fraction of LAGBs in deformed grains in RV-ISF by T3 is observed as compared with that in FS-ISF by T0 despite that the temperature in RV-ISF by T3 is lower. This indicates that the induced localised vibration in RV-ISF enhances the formation of LAGBs, reflecting more

dislocation rearrangement and annihilation, which may be one of the reasons for softening.

5.2. Grain refinement and surface shear effect

As evidenced by the grain distribution and average grain size calculation in Section 4.4, RV-ISF is more effective in refining microstructure of AZ31B-H24 as compared with that by FS-ISF. The microstructure refinement is also reflected by the increased fraction of LAGBs after RV-ISF, where more subgrains form. At the early stage of recrystallisation in the first few cycles of deformation and heating in FS-ISF and RV-ISF, small equiaxed grains are nucleated but only consume a small fraction of the deformed matrix. At this stage, the lower recrystallisation degree in RV-ISF leads to larger average grain sizes. However, at the later stage, the small equiaxed grains grow into larger-sized grains after experiencing several cycles of deformation and heating with the cyclic loading characteristic of ISF. The lower recrystallisation degree in RV-ISF corresponds to smaller average grain sizes in RV-ISF. The less temperature rise and the localised vibration effect may be the reason for the limited grain growth after recrystallisation nucleation, accordingly more microstructure refinement by RV-ISF.

For both RV-ISF and FS-ISF, extremely refined grains and enhanced recrystallisation behaviour are observed on the toolsheet contact interface. In ISF, the sheet material is plastically deformed by the forming tool, while the tool-sheet contact interface experiences additional shear deformation, leading to the gradient of the through-thickness strain distribution, with the highest level on the contact top layer of the sheet thickness, which is reflected by the highest GND as revealed in Section 4.7. This is the driving force for the recrystallisation and grain refinement. The more microstructure refinement by RV-ISF and the extreme surface grain refinement by both RV-ISF and FS-ISF are expected to enhance the material strength after ISF for manufacturing parts with high loading capacity.

6. Conclusions

This study presents a new method to decouple the thermal and vibration softening effect in RV-ISF and provides new insights into the combined softening mechanism by investigating the similarity and difference between FS-ISF and RV-ISF in processing AZ31B-H24. The key conclusions are:

- (1) The thermal and vibration softening effects are decoupled with consideration of the relationship between the vertical forming force and the material flow stress in RV-ISF. For RV-ISF of AZ31B-H24, the thermal effect from the friction heating contributes to the majority of the softening effect within the range of 45∼65%, while the vibration effect provides an additional contribution of up to 15% of the overall softening from the conventional ISF.
- (2) The rotation of the double-offset tool T2 leads to more vibration softening than that by the three-groove tool T3 because of the larger vibration amplitude created by T2 tool.

- With an increase of the tool rotational speed, the thermal softening effect is enhanced, while the vibration softening effect does not have much change.
- (3) Compared with FS-ISF, the AZ31B-H24 samples by RV-ISF with tool T3 and 3000 rpm has more refined microstructure with smaller grain sizes of 0.94 μm , 2.3 μm , 2.19 μm due to the lower recrystallisation degrees of 71.8%, 33.7%, 36.2% at the top, middle, bottom layers of the sheet thickness, respectively, because of the combined effect of lower temperature and local vibration. The considerable surface shearing effect from the contact friction may lead to the extra refinement on the tool-sheet contact surface.
- (4) Compared with FS-ISF, the AZ31B-H24 samples by RV-ISF with tool T3 and 3000 rpm has higher GND density of 4.88 × 10¹⁴, 6.18 × 10¹⁴ and 5.56 × 10¹⁴ m⁻² at the top, middle and bottom layers of the sheet thickness, respectively, due to the less dislocations involved into the grain boundary migration in recrystallisation under the combined effect of lower temperature and local vibration.
- (5) In RV-ISF of AZ31B-H24, the higher fraction of LAGBs in deformed grains of 41.5%, 48.5%, 44.7% at the top, middle, bottom layers of the sheet thickness, respectively, indicates that the enhanced rearrangement and annihilation of dislocations may be one of the reasons for vibration softening effect to take place in the RV-ISF of AZ31B-H24, as it is expected to be reduced at lower temperature in RV-ISF but it is higher instead.

CRediT authorship contribution statement

Hui Zhu: Visualisation, Conceptualisation, Writing – original draft, Validation, Methodology, Investigation. Xiaohan Zeng: Writing – original draft, Visualisation, Methodology, Investigation. Hui Long: Writing – review & editing, Methodology, Funding acquisition, Conceptualisation. João Quinta da Fonseca: Writing – review & editing, Methodology, Funding acquisition.

Declaration of competing interest

The authors declare that there is no conflict of interests regarding the publication of this work.

Acknowledgments

The authors would like to acknowledge the financial support received from the UK Engineering and Physical Sciences Research Council (EPSRC) through project grants EP/W010089/1 and EP/T005254/1.

References

- [1] B.L. Mordike, T. Ebert, Mat. Sci. Eng. A 302 (1) (2001) 37–45, doi:10. 1016/S0921-5093(00)01351-4.
- [2] M.M. Avedesian, H. Baker, ASM specialty handbook-magnesium and magnesium alloys, ASM Int, 1999.

- [3] T. Zhang, W. Wang, J. Liu, L. Wang, Y. Tang, K. Wang, Front. Bioeng. Biotechnol. 10 (2022) 953344, doi:10.3389/fbioe.2022.953344.
- [4] E. Momeni, S. Hassan, T. Morteza, K. Ahmad, A. Ermia, B.Yashar Behnamian, J. Magnes. Alloy. 11 (9) (2023) 3362–3381, doi:10.1016/j.jma.2023.09.006.
- [5] S.K. Moheimani, A. Keshtgar, S. Khademzadeh, M. Tayebi, A. Rajaee, A. Saboori, J. Magnes. Alloy. 10 (11) (2022) 3267–3280, doi:10.1016/ j.jma.2021.05.016.
- [6] S.R. Agnew, Ö. Duygulu, Int. J. Plast. 21 (6) (2005) 1161–1193, doi:10. 1016/j.ijplas.2004.05.018.
- [7] M.H. Yoo, S.R. Agnew, J.R. Morris, K.M. Ho, Mat. Sci. Eng. A 319 (2001) 87–92, doi:10.1016/S0921-5093(01)01027-9.
- [8] M. Tayebi, A.B. Kheradmand, Z. Lalegani, A.R. Eivani, M. Emamy, J. Alloys Compd. 1020 (2025) 179405, doi:10.1016/j.jallcom.2025. 179405
- [9] H. Zhang, X. Chu, C. Liu, X. Sun, S. Lin, Mater. Des. 247 (2024) 113437, doi:10.1016/j.matdes.2024.113437.
- [10] H. Zhang, Y. Ding, R. Li, Y. Gao, J. Mater. Res. Technol. 28 (2024) 1841–1851, doi:10.1016/j.jmrt.2023.12.127.
- [11] H. Zhang, G. Huang, B. Song, L. Zhang, D. Kong, Trans. Nonferr. Met. Soc. China 21 (4) (2011) 844–850, doi:10.1016/S1003-6326(11) 60791-7.
- [12] J. Jeswiet, F. Micari, G. Hirt, A. Bramley, J. Duflou, J. Allwood, CIRP Ann. Manuf. Technol. 54 (2) (2005) 623–649, doi:10.1016/ S0007-8506(07)60021-3.
- [13] H. Zhu, H. Ou, A. Popov, Int. J. Adv. Manuf. Technol. 111 (2020) 565–587, doi:10.1007/s00170-020-06056-5.
- [14] S. Zhang, G. Tang, W. Wang, X. Jiang, Measurement 157 (2020) 107673, doi:10.1016/j.measurement.2020.107673.
- [15] J.R. Duflou, B. Callebaut, J. Verbert, H. De Baerdemaeker, CIRP Ann. Manuf. Technol. 56 (1) (2007) 273–276, doi:10.1016/j.cirp.2007. 05.063.
- [16] P. Lehtinen, T. Väisänen, M. Salmi, Phys. Procedia 78 (2015) 312–319, doi:10.1016/j.phpro.2015.11.045.
- [17] A. Al-Obaidi, V. Kräusel, D. Landgrebe, Int. J. Adv. Manuf. Tech. 82 (5–8) (2016) 1163–1171, doi:10.1007/s00170-015-7439-x.
- [18] G. Ambrogio, F. Gagliardi, A. Chamanfar, W.Z. Misiolek, L. Filice, Int. J. Adv. Manuf. Tech. 91 (1–4) (2017) 803–812, doi:10.1007/s00170-016-9794-7.
- [19] W. Li, M.M. Attallah, K. Essa, J. Mater, Process. Technol. 299 (2022) 117323, doi:10.1016/j.jmatprotec.2021.117323.
- [20] G. Fan, L. Gao, G. Hussain, Z. Wu, Int. J. Mach. Tools Manuf. 48 (15) (2008) 1688–1692, doi:10.1016/j.ijmachtools.2008.07.010.
- [21] D. Ao, J. Gao, X. Chu, S. Lin, J. Lin, Int. J. Solids Struct. 202 (2020) 357–367, doi:10.1016/j.ijsolstr.2020.06.028.
- [22] H. Zhang, X. Chu, W. Bao, J. Gao, L. Chen, Mater. Sci. Eng. A. 823 (2021) 141732, doi:10.1016/j.msea.2021.141732.
- [23] M. Otsu, H. Matsuo, M. Matsuda, K. Takashima, Proc. Metalform. (2010) 942–945.
- [24] X. Zhan, D. An, J. Chen, Int. J. Mach. Tools Manuf. 180 (2022) 103928, doi:10.1016/j.ijmachtools.2022.103928.
- [25] H. Zhu, H. Ou, J. Mater, Process. Technol. 328 (2024) 118396, doi:10. 1016/j.jmatprotec.2024.118396.
- [26] M. Vahdati, R. Mahdavinejad, S. Amini, A. Abdullah, K. Abrinia, Modares Mech. Eng. 14 (11) (2015) 68.
- [27] S. Amini, A.H. Gollo, H. Paktinat, Int. J. Adv. Manuf. Tech. 90 (2017) 1569–1578, doi:10.1007/s00170-016-9458-7.
- [28] P. Li, J. He, Q. Liu, M. Yang, Q. Wang, Q. Yuan, Y. Li, Aerosp. Sci. Technol. 63 (2017) 132–139, doi:10.1016/j.ast.2016.12.028.
- [29] Y. Li, W. Zhai, Z. Wang, X. Li, L. Sun, J. Li, G. Zhao, J. Mater. Res. Technol. 9 (1) (2020) 433–454, doi:10.1016/j.jmrt.2019.10.072.
- [30] Y. Long, Y. Li, J. Sun, I. Ille, J. Li, J. Twiefel, Int. J. Adv. Manuf. Tech. 97 (2018) 13–24, doi:10.1007/s00170-018-1886-0.
- [31] Z. Cheng, Y. Li, J. Li, F. Li, P.A. Meehan, J. Mater. Process. Technol. 299 (2022) 117365, doi:10.1016/j.jmatprotec.2021.117365.
- [32] B. Lu, Z. Li, H. Long, F. Chen, J. Chen, H. Ou, Procedia Eng. 207 (2017) 795–800. https://doi.org/10.1016/j.proeng.2017.10.831.

JID: JMAA ARTICLE IN PRESS [m5+;October 16, 2025;1:54]

H. Zhu, X. Zeng, H. Long et al./Journal of Magnesium and Alloys xxx (xxxx) xxx

[33] S. Wu, P. Geng, N. Ma, F. Lu, J. Mater. Res. Technol. 17 (2022) 1363– 1379, doi:10.1016/j.jmrt.2022.01.103.

26

- [34] Y.K. Dewangan, R. Banjare, K. Bandyopadhyay, Proc. Inst. Mech. Eng. B-J. Eng. Manufact. (2024) 09544054241249208, doi:10.1177/ 09544054241249208.
- [35] H. Long, W. Peng, Z. Chang, H. Zhu, Y. Jiang, Z. Li, J. Mater. Process. Technol. 326 (2024) 118311, doi:10.1016/j.jmatprotec.2024.118311.
- [36] B. Langenecker, IEEE Trans. Sonics Ultrason. 13 (1) (1966) 1–8, doi:10. 1109/T-Su.1966.29367.
- [37] Y. Daud, M. Lucas, Z. Huang, J. Mater, Process. Technol. 186 (1–3) (2007) 179–190, doi:10.1016/j.jmatprotec.2006.12.032.
- [38] K.W. Siu, A.H.W. Ngan, I.P. Jones, Int. J. Plast. 27 (5) (2011) 788–800, doi:10.1016/j.ijplas.2010.09.007.
- [39] R.K. Dutta, R.H. Petrov, R. Delhez, M.J.M. Hermans, I.M. Richardson, A.J. Böttger, Acta Mater 61 (5) (2013) 1592–1602, doi:10.1016/j. actamat.2012.11.036.
- [40] H.O.K. Kirchner, W.K. Kromp, F.B. Prinz, P. Trimmel, Mater. Sci. Eng. 68 (2) (1985) 197–206, doi:10.1016/0025-5416(85)90409-4.
- [41] J. Lin, C. Pruncu, L. Zhu, L. Jiao, Y. Zhai, L. Chen, Y. Guan, G. Zhao, J. Mater. Process. Technol. 299 (2022) 117360, doi:10.1016/j.jmatprotec. 2021.117360.

- [42] H. Sun, W. Zhang, Q. Li, X. Zhuang, Z. Zhao, J. Mater. Process. Technol. 330 (2024) 118487, doi:10.1016/j.jmatprotec.2024.118487.
- [43] T. Liu, J. Lin, Y. Guan, Z. Xie, L. Zhu, J. Zhai, Ultrasonics 89 (2018) 26–33.
- [44] J. Kang, X. Liu, M. Xu, Mater. Sci. Eng A. 785 (2020) 139364.
- [45] B. Meng, B. Cao, M. Wan, C. Wang, D. Shan, Int. J. Mech. Sci. 157 (2019) 609–618.
- [46] G.R. Johnson, in: Proc. 7th Int. Symp. Ballistics, Netherlands, The Hague, 1983.
- [47] D. Fields, W. Backofen, Proc. ASTM 57 (1957) 1259-1272.
- [48] R. Aerens, P. Eyckens, A. Van Bael, J.R. Duflou, Int. J. Adv. Manuf. Tech. 46 (2010) 969–982, doi:10.1007/s00170-009-2160-2.
- [49] H.T. Jeong, T.K. Ha, J. Mater, Process. Technol. 187-188 (2007) 559–561, doi:10.1016/j.jmatprotec.2006.11.084.
- [50] B. Aashranth, M.A. Davinci, D. Samantaray, U. Borah, S.K. Albert, Mater. Des. 116 (2017) 495–503, doi:10.1016/j.matdes.2016.12.053.
- [51] Q. Liu, D.J. Jensen, N. Hansen, Acta Mater. 46 (16) (1998) 5819–5838, doi:10.1016/S1359-6454(98)00229-8.

Please cite this article as: H. Zhu, X. Zeng, H. Long et al., New insights into combined thermal and vibration softening of magnesium alloy in rotational vibration assisted incremental sheet forming, Journal of Magnesium and Alloys, https://doi.org/10.1016/j.jma.2025.09.016